IEEE Transactions on Automation Science and Engineering (T-ASE) paper, presented at ICRA 2026, Vienna, Austria.
Cite as T-ASE paper.

Whole-Body Stabilization of a Cable-Suspended Multirotor Platform Carrying a Slung Load

Hemjyoti Das, *Graduate Student Member, IEEE*, Grazia Zambella, *Member, IEEE*, and Christian Ott, *Fellow, IEEE*

***Abstract*—Suspended multirotor platforms are fascinating systems that can be employed in construction applications to provide safe transportation of heavy loads. Such a system comprising a cable-suspended platform with attached load features seven degrees of freedom (DoF) motion for the whole system. In this paper, we propose a composite whole-body control framework for the stabilization of the suspended multirotor platform system, leveraging singular perturbation theory to exploit the inherent three time-scale dynamics of the system. The control strategy computes the underactuated 3-DoF wrench space generated by the platform's actuation units for the stabilization of the complete system. Building upon this, we develop a superposition-based shared control approach and then compare the two controllers. Moreover, to address specific cases where the time-scale separation between two dynamics of the triple-spherical pendulum becomes negligible, we design an operational space controller. The control approaches are validated using both extensive numerical simulations and experiments in different scenarios. We also carried out numerical robustness and stability analysis of the whole system. Note that our system relies on only onboard sensors for state estimation, which makes it effective for real-life outdoor applications.**

***Note to Practitioners*—This paper is motivated by the transportation of heavy loads using overhead cranes in construction sites. Due to the safety criticality of such applications, it has to be ensured that no oscillations of the attached load arise during the whole process. These oscillations can result from wind disturbances or due to the motion of the crane. In this work, we ensure that the proposed control approaches stabilize the attached load by utilizing the actuation power of an aerial platform suspended from the crane, and thus ensure safety in the involved construction sites. The practical implications of this work are validated using extensive simulation studies and experimental tests in two different lab settings, while demonstrating the numerical stability and robustness of the proposed framework to tackle the different uncertainties and external disturbances that can arise in construction sites.**

***Index Terms*—Composite control, shared control, whole-body control, aerial robots, crane-load stabilization.**

Received 30 June 2024; revised 13 April 2025; accepted 26 May 2025. Date of publication 16 July 2025; date of current version 16 October 2025. This article was recommended for publication by Associate Editor V. Kamat and Editor J. Yi upon evaluation of the reviewers' comments. This work was supported by Austrian Research Promotion Agency (FFG) within the Program Expedition Zukunft through the HängMan Project with FFG Project under Grant FO999913217. *(Corresponding author: Hemjyoti Das.)*

Hemjyoti Das and Grazia Zambella are with the Automation and Control Institute (ACIN), TU Wien, 1040 Vienna, Austria (e-mail: hemjyoti.das@tuwien.ac.at; grazia.zambella@tuwien.ac.at).

Christian Ott is with ACIN, TU Wien, 1040 Vienna, Austria, and also with the Institute of Robotics and Mechatronics, German Aerospace Center (DLR), 82234 Weßling, Germany (e-mail: christian.ott@tuwien.ac.at).

This article has supplementary downloadable material available at https://doi.org/10.1109/TASE.2025.3588767, provided by the authors.

Digital Object Identifier 10.1109/TASE.2025.3588767

I. Introduction

In RECENT years, the use of aerial robots has increased tremendously, both in the research community and in the industries [1]. Such robots have demonstrated various robust capabilities in both indoor and outdoor environments [2] for applications related to load transport, inspection, aerial mapping, and constructions [2], [3], [4]. For some of these applications, a robotic manipulator or a payload is attached to an aerial platform. Such attachments are often limited by their weight and the actuation capability of the platform. Mounting a heavy manipulator might necessitate a large-scale aerial base [5] that can generate a lot of turbulence in close proximity to the ground, and thus raise safety concerns. Additionally, the energy consumed by the aerial base for compensating gravity can restrain its payload capacity and flight time.

To increase payload capability and performance, while mitigating the other aforementioned issues, a cable-suspended aerial manipulator platform (SAM) is proposed in [6]. It consists of a robotic arm attached to a multirotor platform, which is suspended from a crane or an aerial carrier system. The inherent gravity compensation due to the suspension is a major advantage of the platform that has been used to demonstrate various hierarchical compliant tasks with the environment [7], [8]. A similar platform is proposed in [9], which is suspended using elastic cables and is capable of generating a six-DoF wrench. They utilize nonlinear model predictive control (NMPC) to demonstrate accurate trajectory tracking, while minimizing its energy consumption [10], [11]. In [12], [13], a similar platform with a pair of soft robotic hands is proposed, which demonstrates dexterity and robustness in grasping objects while teleoperating in unstructured environments.

The SAM platform is also utilized in [14] to demonstrate a novel telepresence system by the use of a haptic device and virtual reality (VR). Over seventy complex aerial manipulation tasks are demonstrated in [14], achieving a reduction in the execution time by approximately 1.8 times for both pick-and-place and peg-in-hole operations. In [15], the SAM system is augmented with a winch-based actuation in order to generate the desired wrench, based on the cable tension to reduce the effect of the gravitational torque. Similarly, the cable-suspended aerial manipulator developed in [11] is combined with a macrobot in [16] to combine the benefit of its large workspace with the high dynamics of the aerial vehicle. This aerial platform is further utilized in [17] to demonstrate teleop-

IEEE Transactions on Automation Science and Engineering (T-ASE) paper, presented at ICRA 2026, Vienna, Austria.

Fig. 1. Envisioned target application for stabilization of a crane-load system using a suspended underactuated multirotor platform.

eration tasks with a handheld camera, where they introduced the concept of virtual camera + IMU concept (VCI) to improve its efficiency without any hindrance.

Although suspended aerial platforms have been utilized for different applications, the pendulum motion generated due to their suspension is one of the main challenges that needs to be tackled. Such motions have been first analyzed in [18], which considers the suspended platform to behave as a spherical double pendulum. The first spherical joint gives rise to low-frequency and high-amplitude oscillation, whereas the second joint gives rise to high-frequency and low-amplitude oscillation. An optimal control technique is developed in [18] to damp these oscillations; however, it considers a simplified model by assuming the second spherical joint to be in equilibrium while framing the control law. In this paper, we extend the application of such a suspended aerial platform to aid overhead cranes and aerial carrier systems in the transportation of heavy loads by eliminating any induced oscillations.

A suspended aerial platform with an attached slung load requires a different treatment, as compared to a slung load attached to conventional free-flying aerial platforms without any suspension constraints, studied previously in [19], [20], [21], [22], [23], [24], [25], and [26]. For instance, a back-stepping controller is designed for a UAV in [21] to follow a given trajectory while minimizing the oscillations of its attached load. An input-shape filtering is further utilized to generate the reference trajectory for the UAV to minimize its payload swing, which is not applicable for the multirotor platform in this work, as it is suspended from a given point and, therefore, the platform would instead generate counter-movements to destabilize the attached load to achieve its own equilibrium. In [22], the work in [21] is extended to account for wind disturbances through the use of an integral effect, which is also utilized in this work for wind compensation.

Similarly, an adaptive controller is developed in [23] to dampen an unknown payload being attached to the quadrotor, and is validated using simulation studies. It utilizes the elasticity of the rope to further accelerate the swing suppression, in contrast to the approach in this work, which considers a rigid rope. Additionally, adaptive control methods can be computationally complex for our system, which involves multiple time-scale dynamics of our suspended multirotor system. In contrast, an optimization-based trajectory generation approach is proposed in [24] and experimentally validated to stabilize an attached load using a quadrotor. Their control approach relies on changing the cable length using a winch and swing suppression, unlike our approach, which assumes a fixed cable length. A motion capture system is utilized to estimate the pose of the markers attached to the load, contrary to onboard sensors used in this work, thus making our approach more practical for real-world deployment.

Nonlinear control techniques such as nonlinear dynamic inversion (NDI) and a higher-order sliding mode control are utilized in [25] and [26], respectively, to dampen the oscillations of a quadrotor with an attached load, and are verified using simulation studies. These control approaches do not take into account any possible rotor failures, which are considered in this work by virtue of the calculated wrench, which additionally makes our control approach also applicable to omnidirectional platforms. The load attached to these free-flying aerial platforms and their total time-of-flight is severely limited by their actuation capacity, which can be compensated to a great extent by the use of a suspended aerial platform. However, this will necessitate different techniques for the stabilization of the complete system.

In this paper, we formulate the dynamics of a suspended aerial platform with a slung load attached to it. The aerial system is considered to have two modes of oscillation as defined in [18], with the attached load demonstrating its own frequency mode. The complete system thus operates at three different time scales, which are accounted for by our designed composite whole-body controller. Our designed controller considers the underactuated nature of the suspended platform, which can exert a 3-DoF wrench to stabilize the 7-DoF system. However, prior approaches of whole-body controllers such as [15], [27] rely on the full actuation of the SAM system and the KUKA LWR IV+ manipulator, respectively. Other whole-body control approaches for underactuated systems, such as humanoid and quadrupedal robots [28], [29], [30], [31], [32], [33] utilize Quadratic Programming (QP) based optimization with respect to the constraints on system dynamics, contact points, and actuators. Our work does not rely on such optimization-based control techniques, whose primary focus is on handling underactuation, and instead employs a model-based control strategy.

Our control approach does not consider a strict hierarchy for whole-body stabilization due to the involved underactuation. In contrast, prior works such as [7], [8], and [27] consider

IEEE Transactions on Automation Science and Engineering (T-ASE) paper, presented at ICRA 2026, Vienna, Austria.

a strict hierarchy to accomplish different tasks in a way that the higher priority tasks do not interfere with the lower priority tasks. Our composite control approach instead considers different time-scale operations of the complete system dynamics, similar to [34], where the controller for the slow system dynamics considers the equilibrium of its relatively fast dynamics. In [35], a similar problem of load stabilization from a suspended multirotor platform is addressed using a partial feedback linearization approach. However, the approach in [35] did not consider any time-scale separation of the system dynamics and relies on a simplified single-pendulum assumption of the suspension dynamics without accounting for the mounting hook of the crane, which is explicitly modeled in this work. Additionally, this work employs an overhead crane setup as one of the validation platforms, providing a more representative experimental scenario than the indoor laboratory setting considered in [35]. The main contributions of this paper can be summarized as follows

- A novel model-based control architecture based on singular perturbation theory is proposed to dampen the oscillations of the complete system while utilizing the underactuated wrench space of the suspended multirotor platform.
- An additional controller based on shared control is proposed, and its stabilization response and energy consumption are compared with the previous approach.
- Numerical robustness and stability analysis are done for the proposed control approaches, for varying mass of the attached load and external wind disturbances.
- The control approaches are validated using extensive simulation studies and experimental tests.

In this work, we also develop a state estimator based on an extended Kalman filter (EKF) in order to estimate the length of the suspension cable. Consequently, our control approaches rely on only onboard sensors mounted on the platform, which is advantageous for outdoor use, as envisioned in our target application. We also compare the stabilization performance and the energy consumption of the underactuated aerial platform with an omnidirectional aerial platform. Furthermore, we analyze the scalability of the suspended aerial platform, necessary for larger payloads, with its associated change in the controller gains for smooth stabilization. Additionally, an operational space controller is developed specifically for the overhead crane setup to handle special cases of the triple spherical pendulum dynamics where the time-scale separation between the two spherical joints of the crane diminishes.

The rest of the paper is organized as follows. Section II presents a brief overview of the complete system and its dynamic model. In section III, the proposed controllers are presented, while the estimation algorithms are summarized in section IV. The validation results in simulations and experiments are presented in section V and VI, respectively. Finally, section VII concludes the paper and presents the future work.

II. System Overview and Modelling

In this section, we first explain the system dynamics of the suspended aerial platform with the attached load, following which we introduce the underactuated multirotor platform used in this work.

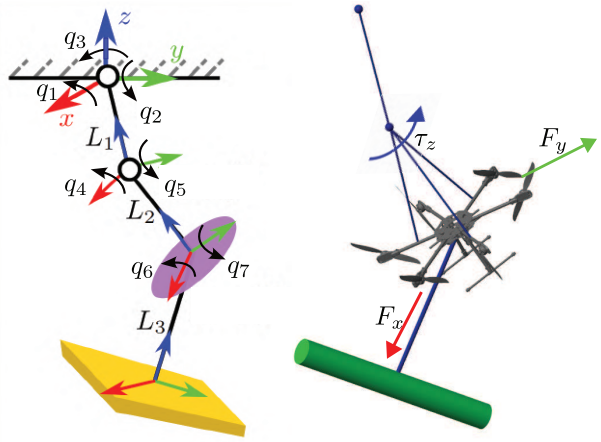

Fig. 2. Schematic representation of the suspended aerial platform with the attached load (on left) and the actual simulated system (on right). Note that the second and the third spherical joints do not rotate about their respective z axis due to their mechanical constraints.

A. System Dynamics

The multirotor platform (Fig. 1) considered in this paper can be suspended from an overhead crane [6] or an aerial carrier system [5]. The overall system, consisting of the suspended multirotor platform with the attached slung load, is modeled as a spherical triple pendulum (Fig. 2). The first spherical joint has three DoFs, which are the rotation of the first cable of length L_1, about its x, y, and z axes, denoted by q_1, q_2, and q_3, respectively. The second joint consists of two DoFs, namely q_4 and q_5, which are the rotation of the cable with length L_2 about its x and y axes, respectively. Due to constraints in the suspension mechanism, we do not consider any rotation about its z axis, similar to [36]. Additionally, we assume that the cables used for suspension are always taut, similar to the works in [6] and [7]. The load suspended from the platform demonstrates the dynamics of a spherical pendulum with two DoFs, which are the rotation of the third cable with length L_3 about its x and y axes, denoted by q_6 and q_7, respectively. Similar to the second spherical joint and for the same reasons, we assume no rotation of the attached load about its z axis. The complete system is thus described by seven DoFs, and its dynamics are summarized as

$$\mathbf{M}(\mathbf{q})\ddot{\mathbf{q}} + \mathbf{C}(\mathbf{q}, \dot{\mathbf{q}})\dot{\mathbf{q}} + \mathbf{g}(\mathbf{q}) = \boldsymbol{\tau}, \tag{1}$$

where $\mathbf{q} = \begin{bmatrix} q_1 & q_2 & q_3 & q_4 & q_5 & q_6 & q_7 \end{bmatrix}^T$ represents the joint-configuration vector of the complete system. The matrices $\mathbf{M}(\mathbf{q}) \in \mathbb{R}^{7\times7}$ and $\mathbf{C}(\mathbf{q}, \dot{\mathbf{q}}) \in \mathbb{R}^{7\times7}$ are the inertia and centrifugal/Coriolis matrix, respectively. The vector $\mathbf{g}(\mathbf{q}) \in \mathbb{R}^7$ represents the gravity vector, and $\boldsymbol{\tau} \in \mathbb{R}^7$ denotes the applied torque at the joints. The 3D wrench commanded by the controller is denoted by $\mathbf{u} \in \mathbb{R}^3$, which is related to the joint-torque $\boldsymbol{\tau}$ using the Jacobian $\mathbf{J}(\mathbf{q}) \in \mathbb{R}^{3\times7}$ as $\boldsymbol{\tau} = \mathbf{J}(\mathbf{q})^T\mathbf{u}$. For the sake of clarity in notations, the configuration and velocity dependencies of the terms will be omitted from this point on.

IEEE Transactions on Automation Science and Engineering (T-ASE) paper, presented at ICRA 2026, Vienna, Austria.

The complete system operates at three different time-scale dynamics, which are classified into fast, medium-fast, and slow dynamics. Their corresponding coordinates are represented as $\mathbf{q}_f$, $\mathbf{q}_m$ and $\mathbf{q}_s$, respectively, as shown below:

$$\mathbf{q}_f = \begin{bmatrix} q_4 & q_5 \end{bmatrix}^T, \ \mathbf{q}_m = \begin{bmatrix} q_6 & q_7 \end{bmatrix}^T, \ \mathbf{q}_s = \begin{bmatrix} q_1 & q_2 & q_3 \end{bmatrix}^T. \tag{2}$$

The time-scale of operation of the different joints is dependent on the length of the cables and inertial properties of the suspended platform and the attached load, which led to their categorization into the three classes. For the suspended platform without the attached load, it has been analyzed in [18] that the second spherical joint $\mathbf{q}_f$ is faster than the first spherical joint $\mathbf{q}_s$. Additionally, for our system, we consider the attached slung load to have an intermediate time-scale of operation, as compared to the two other dynamics. However, increasing the length of L_3 makes the load dynamics slower, and vice versa. It has also been found that increasing the length of L_1 increases the frequency separation between the slow and medium-fast dynamics, and vice versa.

Next, we define the following matrices by inverting the inertia matrix in (1) as

$$\begin{aligned} \begin{bmatrix} \boldsymbol{\gamma}_s & \boldsymbol{\gamma}_f & \boldsymbol{\gamma}_m \end{bmatrix}^T &= \mathbf{M}^{-1}\mathbf{C}\dot{\mathbf{q}} \\ \begin{bmatrix} \boldsymbol{\rho}_s & \boldsymbol{\rho}_f & \boldsymbol{\rho}_m \end{bmatrix}^T &= \mathbf{M}^{-1}\mathbf{g} \\ \begin{bmatrix} \boldsymbol{\lambda}_s & \boldsymbol{\lambda}_f & \boldsymbol{\lambda}_m \end{bmatrix}^T &= \mathbf{M}^{-1}\mathbf{J}^T, \end{aligned} \tag{3}$$

where the components $\boldsymbol{\gamma}_s \in \mathbf{R}^3$, $\boldsymbol{\gamma}_f \in \mathbf{R}^2$ and $\boldsymbol{\gamma}_m \in \mathbf{R}^2$ are the transformed centrifugal/Coriolis components for the respective sub-systems. Similarly, the vectors $\boldsymbol{\rho}_s \in \mathbf{R}^3$, $\boldsymbol{\rho}_f \in \mathbf{R}^2$ and $\boldsymbol{\rho}_m \in \mathbf{R}^2$ are the transformed gravity vectors. The matrices $\boldsymbol{\lambda}_s \in \mathbf{R}^{3\times3}$, $\boldsymbol{\lambda}_f \in \mathbf{R}^{2\times3}$ and $\boldsymbol{\lambda}_m \in \mathbf{R}^{2\times3}$ can be considered as the effective control matrices for each subsystem. These dynamic matrices $\boldsymbol{\lambda}_s$, $\boldsymbol{\lambda}_m$ and $\boldsymbol{\lambda}_f$ are always non-singular in our case due to given selection of the generalized coordinates. Utilizing the dynamic components in Eq. (3), we rewrite the system in (1) in the state-space form for the three subsystems as

$$\dot{\mathbf{x}}_s = \begin{bmatrix} \dot{\mathbf{q}}_s \\ \ddot{\mathbf{q}}_s \end{bmatrix} = \begin{bmatrix} \dot{\mathbf{q}}_s \\ -\boldsymbol{\gamma}_s - \boldsymbol{\rho}_s + \boldsymbol{\lambda}_s\mathbf{u} \end{bmatrix} \tag{4a}$$

$$\dot{\mathbf{x}}_m = \begin{bmatrix} \dot{\mathbf{q}}_m \\ \ddot{\mathbf{q}}_m \end{bmatrix} = \begin{bmatrix} \dot{\mathbf{q}}_m \\ -\boldsymbol{\gamma}_m - \boldsymbol{\rho}_m + \boldsymbol{\lambda}_m\mathbf{u} \end{bmatrix} \tag{4b}$$

$$\dot{\mathbf{x}}_f = \begin{bmatrix} \dot{\mathbf{q}}_f \\ \ddot{\mathbf{q}}_f \end{bmatrix} = \begin{bmatrix} \dot{\mathbf{q}}_f \\ -\boldsymbol{\gamma}_f - \boldsymbol{\rho}_f + \boldsymbol{\lambda}_f\mathbf{u} \end{bmatrix}. \tag{4c}$$

B. Underactuated Planar-Thrust Platform

In this work, we utilize an underactuated planar-thrust aerial platform [36] to exert the 3D wrench $\mathbf{u}$, which is composed of the translational force along the x and y axes, denoted as F_x and F_y, respectively. The third component τ_z is the torque about the z axis. The wrench vector $\mathbf{u}$ can be summarized as

$$\mathbf{u} = \begin{bmatrix} F_x & F_y & \tau_z \end{bmatrix}^T. \tag{5}$$

This platform has six actuation units that can exert a planar thrust necessary for the stabilization of the complete system. Unlike an omnidirectional aerial platform used in most works [6], [7], [11], [15], utilizing such an underactuated mechanism allows us to conserve the total actuation energy necessary for the stabilization of the complete system. The six unidirectional thrusters are installed at an angle of ±90 degrees about the radial axis of the platform, with the direction of each thrusters shown in Fig. 3. Due to the involved underactuation of the platform, the wrenches that cannot be exerted by the platform are F_z, τ_x, and τ_y. F_z is the translational force along the z axis, whereas τ_x and τ_y are the rotational torques about the x and y axis, respectively. The applied thrust by the motors is denoted by the vector $\mathbf{F}_m$ defined as

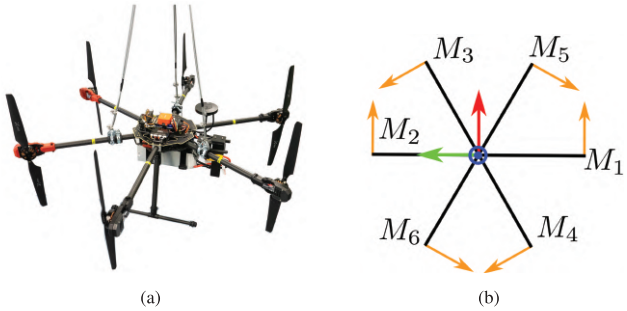

Fig. 3. (a) Suspended planar-thrust underactuated multirotor platform and (b) its top-view where the arrows depict the direction of propulsion, with M_i denoting the i^{th} motor.

$$\mathbf{F}_m = \begin{bmatrix} F_1 & F_2 & F_3 & F_4 & F_5 & F_6 \end{bmatrix}^T, \tag{6}$$

where F_i denotes the thrust generated by the i^{th} motor. The 3D wrench $\mathbf{u}$ exerted by the platform is denoted by $\mathbf{u}_p$, which is related to the motor forces $\mathbf{F}_m$ using the allocation matrix as

$$\mathbf{u}_p = \mathbf{A}_p\mathbf{F}_m \tag{7}$$

The allocation matrix is dependent on the placement of the motors and the length of the arms, summarized as

$$\mathbf{A}_p = \begin{bmatrix} 1 & 1 & -0.5 & -0.5 & -0.5 & -0.5 \\ 0 & 0 & 0.86 & 0.86 & -0.86 & -0.86 \\ 0.4 & -0.4 & 0.4 & -0.4 & -0.4 & 0.4 \end{bmatrix}. \tag{8}$$

In our experimental setup, the motors are commanded with a desired normalized speed signal, which relates to the motor forces using its force coefficient. This force coefficient is obtained using a system identification method. The commanded signal ω_i for the i^{th} motor is thus related to the motor force F_i as

$$\omega_i = aF_i^4 + bF_i^3 + cF_i^2 + dF_i + e, \tag{9}$$

where the coefficients a, b, c, d, and e are -0.05252, 1.399, -13.69, 107.2, and 979.5, respectively. The propellers in our underactuated platform are unidirectional, and therefore, only positive thrust can be commanded to them. Furthermore, the commanded thrust by the actuation units should not exceed the maximum limit of the possible motor thrust $\mathbf{F}_{max}$, which is ensured by solving the following least-squares optimization similar to [36] as

$$\begin{aligned} &\min_{\mathbf{F}_m} \ \|\mathbf{F}_m\|_2^2 \\ &\text{s.t. } \mathbf{A}_p\mathbf{F}_m = \mathbf{u}, \end{aligned}$$

IEEE Transactions on Automation Science and Engineering (T-ASE) paper, presented at ICRA 2026, Vienna, Austria.

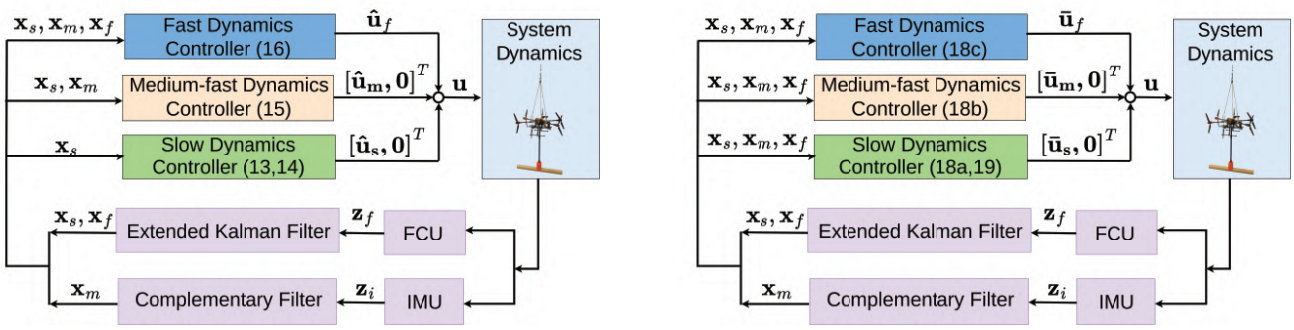

(a) Composite Approach (b) Superposition Approach

Fig. 4. Block diagram of the proposed control approaches.

$$0 \leq \mathbf{F}_m \leq \mathbf{F}_{max} \ . \tag{10}$$

III. Whole-Body Stabilization Control

In this section, we first discuss the fundamentals of the composite control based on [37], following which we design a whole-body controller for the suspended platform with an attached slung load. We then introduce our proposed superposition approach for the stabilization of the complete system.

A. Fundamentals of Composite Control

Composite feedback control [37] is an approach that involves controller design for different dynamics of the complete system and then combining them to obtain the total control command. This framework proposed in [37] considers a system dynamics of the form

$$\begin{aligned} \dot{\mathbf{x}} &= \mathbf{f}(\mathbf{x}, \mathbf{z}, \mathbf{u_c}) \\ \dot{\mathbf{z}} &= \mu \mathbf{g}(\mathbf{x}, \mathbf{z}, \mathbf{u_c}), \end{aligned} \tag{11}$$

where the dynamics of the state $\mathbf{x} \in \mathbf{R}^n$ is considered slower than the dynamics of the state $\mathbf{z} \in \mathbf{R}^m$. The ratio of their time-scales is represented by μ ($\mu \gg 1$). The composite control $\mathbf{u}_c \in \mathbf{R}^r$ is obtained by summing the slow and fast control, denoted by $\mathbf{u}_s$ and $\mathbf{u}_f$, respectively. The slow control $\mathbf{u}_s$ is designed with the hypothesis that the faster system dynamics is at equilibrium, i.e. $\dot{\mathbf{z}} = \mathbf{0}$. Next, the control input $\mathbf{u}_f$ is designed to stabilize the fast dynamics in its equilibrium, which is the unique solution of

$$\mathbf{0} = \mathbf{g}\left(\mathbf{x}, \mathbf{z}, \mathbf{u}_s + \mathbf{u}_f\right) \ . \tag{12}$$

A Lyapunov function candidate is proposed in [37] in order to analyze the stability of both the slow and the fast systems, under the influence of the control inputs $\mathbf{u}_s$ and $\mathbf{u}_f$, respectively. Then, the Lyapunov function of the whole system with a set of interconnection conditions is defined to guarantee the stability of the complete system under the influence of the control $\mathbf{u}_c = \mathbf{u}_s + \mathbf{u}_f$.

This stability framework is applied to the whole-body stabilization of a wheel-based humanoid robot in [34], which is based on composite feedback control. Inspired by this work, we apply the singular perturbation control framework to control a suspended aerial platform with an attached slung load. As in [34], we will not explicitly consider the ratio of the time-scale separation between the different dynamics, represented by μ in (11).

B. Composite Control of the Suspended Platform With an Attached Load

In this work, we stabilize the complete system about its equilibrium $\dot{\mathbf{q}}_s$, $\dot{\mathbf{q}}_m$, $\dot{\mathbf{q}}_f$, $\mathbf{q}_s$ $\mathbf{q}_m$, $\mathbf{q}_f = 0$. All the control goals are thus compatible with the equilibrium, as will be discussed in this section.

1) Slow Dynamics Control: We first design the control input $\mathbf{u} = \hat{\mathbf{u}}_s$ for the slow dynamics, which can be expressed as

$$\hat{\mathbf{u}}_s = \hat{\lambda}_s^{-1}\left(\hat{\mathbf{K}}_{ds}\dot{\tilde{\mathbf{q}}}_s + \hat{\mathbf{K}}_{ps}\tilde{\mathbf{q}}_s + \hat{\boldsymbol{\gamma}}_s + \hat{\boldsymbol{\rho}}_s\right), \tag{13}$$

where $\hat{\lambda}_s \in \mathbf{R}^{3\times3}$, $\hat{\boldsymbol{\gamma}}_s \in \mathbf{R}^3$ and $\hat{\boldsymbol{\rho}}_s \in \mathbf{R}^3$ are obtained from (4a) after assuming that the medium-fast and fast dynamics are in equilibrium, i.e. $\dot{\mathbf{q}}_m$, $\dot{\mathbf{q}}_f$, $\mathbf{q}_m$, $\mathbf{q}_f = 0$. In (13), $\hat{\mathbf{K}}_{ps}$ and $\hat{\mathbf{K}}_{ds}$ are the gains of the controller, while $\tilde{\mathbf{q}}_s$ represent the errors of slow joint $\mathbf{q}_s$ from its reference $\mathbf{q}_s^d = 0$. The performance of the designed feedback linearization controller depends on the accuracy of the dynamic model. Therefore, to reduce the controller dependency on the model and eliminate the strong coupling effects, we designed a PD controller for the slow dynamics as

$$\hat{\mathbf{u}}_s = \hat{\mathbf{J}}_s^{-T}\left(\hat{\mathbf{K}}_{ds}\dot{\tilde{\mathbf{q}}}_s + \hat{\mathbf{K}}_{ps}\tilde{\mathbf{q}}_s\right), \tag{14}$$

where $\hat{\mathbf{J}}_s$ is the component of the Jacobian $\mathbf{J}$ corresponding to the slow variable, extracted after assuming the equilibrium conditions of the fast and the medium-fast dynamics. The experiments conducted in this paper will compare both the feedback linearization and the PD control techniques for the slow dynamics. Note that for damping the complete system about its origin, gravity compensation is not necessary for our controller due to its stabilizing effect.

2) Medium-Fast Dynamics Control: The control input $\mathbf{u} = \hat{\mathbf{u}}_m$ for the dynamics of $\mathbf{q}_m$ is designed as

$$\hat{\mathbf{u}}_m = \hat{\lambda}_m^{-1}\left(\hat{\mathbf{K}}_{dm}\dot{\tilde{\mathbf{q}}}_m + \hat{\mathbf{K}}_{pm}\tilde{\mathbf{q}}_m + \hat{\boldsymbol{\gamma}}_m + \hat{\boldsymbol{\rho}}_m\right), \tag{15}$$

where $\hat{\mathbf{K}}_{dm}$ and $\hat{\mathbf{K}}_{pm}$ are the gains of the controller. The error between the desired joint-position $\mathbf{q}_m^d = 0$ and the actual joint-position $\mathbf{q}_m$ is represented by $\tilde{\mathbf{q}}_m$. The matrices $\hat{\lambda}_m \in \mathbf{R}^{2\times2}$, $\hat{\boldsymbol{\gamma}}_m \in \mathbf{R}^2$ and $\hat{\boldsymbol{\rho}}_m \in \mathbf{R}^2$ are extracted from (4b) by assuming that

IEEE Transactions on Automation Science and Engineering (T-ASE) paper, presented at ICRA 2026, Vienna, Austria.

the fast dynamics is in equilibrium. Additionally, we consider that the dynamics of $\mathbf{q}_m$ is influenced only by the wrenches F_x and F_y, while the torque τ_z has no significant impact on it. Therefore $\hat{\boldsymbol{\lambda}}_m$ disregards the third element of the matrix $\boldsymbol{\lambda}_m$ which corresponds to the torque τ_z. The designed control input $\hat{\mathbf{u}}_m$ is a function of both $\mathbf{x}_m$ and $\mathbf{x}_s$, as $\hat{\boldsymbol{\lambda}}_m$, $\hat{\boldsymbol{\gamma}}_m$ and $\hat{\boldsymbol{\rho}}_m$ are dependent on both of them. Note that PD control is not designed for the medium-fast dynamics, as extracting the diagonal matrices similar to (14) will remove any dependency of the slow variables on the medium-fast dynamics, necessary for the composite control approach. For a similar reason, PD control will also not be designed for the fast dynamics.

3) Fast Dynamics Control: We can express the control input $\mathbf{u} = \hat{\mathbf{u}}_f$ for the dynamics of $\mathbf{q}_f$ as

$$\hat{\mathbf{u}}_f = \hat{\boldsymbol{\lambda}}_f^{-1}\left(\hat{\mathbf{K}}_{df}\dot{\tilde{\mathbf{q}}}_f + \hat{\mathbf{K}}_{pf}\tilde{\mathbf{q}}_f + \boldsymbol{\gamma}_f + \boldsymbol{\rho}_f\right), \tag{16}$$

where $\hat{\mathbf{K}}_{pf}$ and $\hat{\mathbf{K}}_{df}$ are the gains of the controller. The error between the desired and the actual joint position is represented as $\tilde{\mathbf{q}}_f$. The matrix $\hat{\boldsymbol{\lambda}}_f \in \mathbf{R}^{2\times 2}$ is extracted from (4c) by assuming the dynamics of $\mathbf{q}_f$ to be influenced only by the forces F_x and F_y, with τ_z having negligible impact on it. The designed control $\hat{\mathbf{u}}_f$ is thus a function of the states $\mathbf{x}_f$, $\mathbf{x}_m$ and $\mathbf{x}_s$ due to the matrices $\hat{\boldsymbol{\lambda}}_f$, $\boldsymbol{\gamma}_f$ and $\boldsymbol{\rho}_f$.

4) Composite Control Input: Finally, the total control input is obtained as

$$\mathbf{u} = \hat{\mathbf{u}}_s + \begin{bmatrix}\hat{\mathbf{u}}_m & 0\end{bmatrix}^T + \begin{bmatrix}\hat{\mathbf{u}}_f & 0\end{bmatrix}^T . \tag{17}$$

Note that $\mathbf{u}$ is the actual control input that is applied to the system and is thus responsible for stabilizing the complete system. The block diagram of the composite control approach is shown in Fig. 4.

C. Proposed Superposition Control

Our proposed superposition approach is based on the concept of shared control [38], [39], which is commonly used for combining the control of different agents in human-robot collaboration. It involves combining the input from the robot and a human for performing the same task, using a blending policy. In this paper, we design the superposition control in a similar way to the composite control, where we utilize a feedback-linearization controller for each time-scale dynamics, following which we superpose them to obtain the final control command. We represent the designed control-commands for the dynamics of $\mathbf{q}_s$, $\mathbf{q}_m$ and $\mathbf{q}_f$ as $\overline{\mathbf{u}}_s$, $\overline{\mathbf{u}}_m$ and $\overline{\mathbf{u}}_f$, respectively, which are expressed as

$$\overline{\mathbf{u}}_s = \boldsymbol{\lambda}_s^{-1}\left(\overline{\mathbf{K}}_{ds}\dot{\tilde{\mathbf{q}}}_s + \overline{\mathbf{K}}_{ps}\tilde{\mathbf{q}}_s + \boldsymbol{\gamma}_s + \boldsymbol{\rho}_s\right) \tag{18a}$$

$$\overline{\mathbf{u}}_m = \overline{\boldsymbol{\lambda}}_m^{-1}\left(\overline{\mathbf{K}}_{dm}\dot{\tilde{\mathbf{q}}}_m + \overline{\mathbf{K}}_{pm}\tilde{\mathbf{q}}_m + \boldsymbol{\gamma}_m + \boldsymbol{\rho}_m\right) \tag{18b}$$

$$\overline{\mathbf{u}}_f = \overline{\boldsymbol{\lambda}}_f^{-1}\left(\overline{\mathbf{K}}_{df}\dot{\tilde{\mathbf{q}}}_f + \overline{\mathbf{K}}_{pf}\tilde{\mathbf{q}}_f + \boldsymbol{\gamma}_f + \boldsymbol{\rho}_f\right), \tag{18c}$$

where $\overline{\mathbf{K}}_{ps}$, $\overline{\mathbf{K}}_{pm}$, $\overline{\mathbf{K}}_{pf}$, $\overline{\mathbf{K}}_{ds}$, $\overline{\mathbf{K}}_{dm}$ and $\overline{\mathbf{K}}_{df}$ are the gains of the controller. The matrices $\overline{\boldsymbol{\lambda}}_m$ and $\overline{\boldsymbol{\lambda}}_f$ are extracted from (4b) and (4c) by assuming that their corresponding dynamics are influenced only by the forces F_x and F_y, with the torque τ_z having negligible influence on them. The transformed Coriolis, gravity, and the control effectiveness matrices in this approach are thus obtained without utilizing the equilibrium conditions, unlike the composite control approach. Additionally, we also design a PD controller for the slow dynamics similar to (14) as follows

$$\overline{\mathbf{u}}_s = \mathbf{J}_s^{-T}\left(\overline{\mathbf{K}}_{ds}\dot{\tilde{\mathbf{q}}}_s + \overline{\mathbf{K}}_{ps}\tilde{\mathbf{q}}_s\right), \tag{19}$$

where $\mathbf{J}_s$ is the component of the Jacobian $\mathbf{J}$, corresponding to the slow variable. The final control command is then obtained similarly to (17) as

$$\mathbf{u} = \overline{\mathbf{u}}_s + \begin{bmatrix}\overline{\mathbf{u}}_m & 0\end{bmatrix}^T + \begin{bmatrix}\overline{\mathbf{u}}_f & 0\end{bmatrix}^T . \tag{20}$$

D. Operational Space Controller

This section presents a control strategy based on the operational space of the complete system, as outlined earlier. This controller extends the composite and shared control approaches discussed previously, leveraging the system dynamics described in (4a)-(4c). The overall system is modeled as a triple spherical pendulum, with dynamics evolving across distinct time scales: slow, medium-fast, and fast. This timescale separation inherent to triple pendulum models depends on the mass and inertia distribution of the system components. In scenarios where the intermediate body (e.g., the crane hook) has a non-negligible mass relative to the platform or the attached load, the dynamics of the first spherical joints $\mathbf{q}_s$ and the second spherical joints $\mathbf{q}_f$ evolve on comparable time scales. This is indeed the case for the overhead crane setup considered in this work. In such scenarios, a single control law can be derived based on their combined dynamics, with an additional control law for stabilizing the load dynamics. However, due to the involved underactuated wrench space, the inversion of the combined control effectiveness matrix $\boldsymbol{\lambda}_{sf} \in \mathbb{R}^{5\times 3}$, where $\boldsymbol{\lambda}_{sf} = \begin{bmatrix}\boldsymbol{\lambda}_s & \boldsymbol{\lambda}_f\end{bmatrix}^T$ cannot be inverted in the same manner as the previously proposed superposition and shared control approaches.

In order to counteract this issue, we design an operational space controller, where we define the operational space coordinates $\mathbf{x}_o \in \mathbb{R}^3$ and $\mathbf{x}_l \in \mathbb{R}^2$ as

$$\begin{aligned}\mathbf{x}_o &= \begin{bmatrix}x & y & \psi\end{bmatrix}^T \\ \mathbf{x}_l &= \begin{bmatrix}q_6 & q_7\end{bmatrix}^T,\end{aligned} \tag{21}$$

where x and y are the positions of the platform with respect to the suspension point, whereas ψ is the yaw rotation of the platform about the z axis. The operational space $\mathbf{x}_l$ consists of the load joints q_6 and q_7. Next, we obtain a nullspace Jacobian matrix $\mathbf{N} \in \mathbb{R}^{2\times 7}$ similar to [40] and define its associated nullspace velocity $\mathbf{v}_n \in \mathbb{R}^2$ as

$$\mathbf{v}_n = \mathbf{N}\dot{\mathbf{q}} . \tag{22}$$

The nullspace operator ensures an inertial decoupling between the operational space and the nullspace dynamics of $\mathbf{v}_n$. Finally, by utilizing the definition of the Jacobian $\mathbf{J}$ and the nullspace Jacobian $\mathbf{N}$, we can transform the system dynamics (1) similar to [41] as

$$\bar{\mathbf{M}}\ddot{\mathbf{x}} + \bar{\mathbf{C}}\dot{\tilde{\mathbf{q}}} + \bar{\mathbf{g}} = \bar{\mathbf{J}}^T\mathbf{u}, \tag{23}$$

IEEE Transactions on Automation Science and Engineering (T-ASE) paper, presented at ICRA 2026, Vienna, Austria.

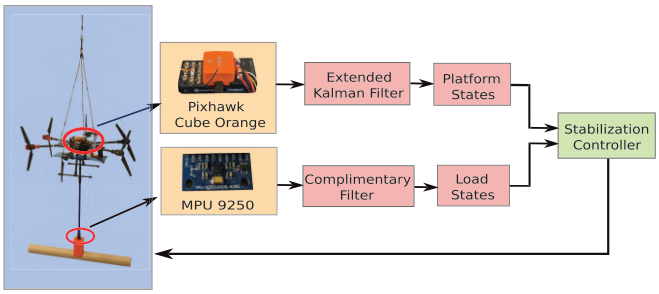

Fig. 5. Experimental platform with the attached load and different sensor boards used for the different state estimation algorithms.

where we define the transformed coordinates $\dot{\bar{\mathbf{x}}} \in \mathbb{R}^7$, the transformed Jacobian $\bar{\mathbf{J}} \in \mathbb{R}^{3\times 7}$ and the inertial matrices $\bar{\mathbf{M}} \in \mathbb{R}^{7\times 7}$, $\bar{\mathbf{C}} \in \mathbb{R}^{7\times 7}$ and $\bar{\mathbf{g}} \in \mathbb{R}^7$ as

$$\begin{aligned}
\dot{\bar{\mathbf{x}}} &= \begin{bmatrix}\dot{\mathbf{x}}_o & \dot{\mathbf{x}}_l & \mathbf{v}_n\end{bmatrix}^T \\
\bar{\mathbf{M}} &= \begin{bmatrix}\mathbf{M}_{oo} & \mathbf{M}_{ol} & \mathbf{0}_{3\times 2} \\ \mathbf{M}_{lo} & \mathbf{M}_{ll} & \mathbf{0}_{2\times 2} \\ \mathbf{0}_{2\times 3} & \mathbf{0}_{2\times 2} & \mathbf{M}_{nn}\end{bmatrix} \\
\bar{\mathbf{C}} &= \begin{bmatrix}\mathbf{C}_{oo} & \mathbf{C}_{ol} & \mathbf{C}_{on} \\ \mathbf{C}_{lo} & \mathbf{C}_{ll} & \mathbf{C}_{ln} \\ \mathbf{C}_{no} & \mathbf{C}_{nl} & \mathbf{C}_{nn}\end{bmatrix} \\
\bar{\mathbf{g}} &= \begin{bmatrix}\mathbf{g}_o & \mathbf{g}_l & \mathbf{g}_n\end{bmatrix}^T \\
\bar{\mathbf{J}} &= \begin{bmatrix}\mathbf{J}_o & \mathbf{J}_l & \mathbf{N}\end{bmatrix}^T,
\end{aligned} \tag{24}$$

where the subscript $\mathbf{M}_{oo} \in \mathbb{R}^{3\times 3}$ is the principal inertial component of the operational space of $\mathbf{x}_o$, whereas $\mathbf{M}_{ol} \in \mathbb{R}^{3\times 2}$ is the cross-coupling inertia element, and defines the contribution of the dynamics of $\mathbf{x}_l$ on the dynamics of $\mathbf{x}_o$. All the other terms in (24) can be defined accordingly, with o, l, and n in the subscripts corresponding to the task coordinate, load states, and the nullspace component, respectively. Next, we derive the respective control law $\mathbf{u}_o$ and $\mathbf{u}_l$ for the states $\mathbf{x}_o$ and $\mathbf{x}_l$, similar to (19) and (18b) as

$$\begin{aligned}
\mathbf{u}_o &= \mathbf{J}_o^{-T}\left(\mathbf{K}_{do}\dot{\tilde{\mathbf{x}}}_o + \mathbf{K}_{po}\tilde{\mathbf{x}}_o\right) \\
\mathbf{u}_l &= \boldsymbol{\lambda}_l^{-1}\left(\mathbf{K}_{dl}\dot{\tilde{\mathbf{x}}}_l + \mathbf{K}_{pl}\tilde{\mathbf{x}}_l + \boldsymbol{\gamma}_l + \boldsymbol{\rho}_l\right),
\end{aligned} \tag{25}$$

where $\mathbf{K}_{do}$, $\mathbf{K}_{po}$, $\mathbf{K}_{dl}$ and $\mathbf{K}_{pl}$ are the control gains, whereas the inertial components of the load dynamics $\boldsymbol{\lambda}_l$, $\boldsymbol{\gamma}_l$ and $\boldsymbol{\rho}_l$ are obtained similar to (3). The total control input is obtained similarly to the superposition approach by summing the two control laws in (25). Note that a separate controller is not designed for the nullspace dynamics due to its inertial decoupling from both the attached load and the operational space dynamics, as well as the inherent underactuation of the system. Its Coriolis-coupled components can, in fact, affect the stabilization performance, but it is very minimal when the mass of the suspension hook is significant, like in the case of our overhead crane system.

IV. State Estimation

In this section, we design an extended Kalman filter (EKF) in order to estimate the states of the platform, similar to [36]. Additionally, we also estimate the length of the cable used for suspending the aerial platform. Due to the suspension from the crane, only the length of the first cable can change, with the two other cables attached to the platform and the attached load having a fixed length. Therefore, we only estimate the length of the first cable due to the involved uncertainties. Similar to [36], we utilize a continuous-discrete EKF due to the involved sensor measurements obtained at discrete time intervals, while the process model (1) is represented using a continuous-time differential equation. We extend the state-space $\hat{\mathbf{x}}$ used in [36] for the estimation of the cable length, summarized as

$$\hat{\mathbf{x}} = \begin{bmatrix}\mathbf{q}_s & \mathbf{q}_f & \dot{\mathbf{q}}_s & \dot{\mathbf{q}}_f & L_1\end{bmatrix}^T \tag{26}$$

The state-space dynamics can be summarized as

$$\dot{\hat{\mathbf{x}}} = \mathbf{f}(\hat{\mathbf{x}}, u) = \begin{bmatrix}\dot{\mathbf{q}}_s \\ \dot{\mathbf{q}}_f \\ \mathbf{f}_s(\hat{\mathbf{x}}, \mathbf{u}) \\ \mathbf{f}_f(\hat{\mathbf{x}}, \mathbf{u}) \\ 0\end{bmatrix} \tag{27}$$

Note that the states of the attached load $\mathbf{q}_m$ and $\dot{\mathbf{q}}_m$ are not estimated by the EKF, which is done by a complementary filter, as will be discussed later in this section. The state-transition function $\mathbf{f}_s(\hat{\mathbf{x}}, \mathbf{u}) \in \mathbf{R}^3$ and $\mathbf{f}_f(\hat{\mathbf{x}}, \mathbf{u}) \in \mathbf{R}^2$ are thus extracted from the system dynamics (1), without considering the load dynamics. The correction of the estimated states using sensor observations will account for these unmodelled dynamics, along with the involved model uncertainties. The prediction of the error covariance matrix $\mathbf{P} \in \mathbf{R}^{11\times 11}$ can be summarized as

$$\dot{\mathbf{P}} = \mathbf{F}\mathbf{P} + \mathbf{P}\mathbf{F}^T + \mathbf{Q}, \tag{28}$$

where $\mathbf{F} \in \mathbf{R}^{11\times 11}$ is the Jacobian of $\mathbf{f}$ with respect the state vector $\hat{\mathbf{x}}$. The process noise is represented by its covariance matrix $\mathbf{Q} \in \mathbf{R}^{11\times 11}$. For the correction step of the EKF, we consider the measurements of the translational velocity and orientation of the platform obtained from the flight controller unit (FCU), similar to [36]. The measurement vector $\mathbf{z_f} \in \mathbf{R}^6$ is summarized as

$$\mathbf{z}_f = \begin{bmatrix}v_x & v_y & v_z & \phi & \theta & \psi\end{bmatrix}^T, \tag{29}$$

where v_x, v_y and v_z are the translational velocities of the platform along its x, y and z axis, respectively. The Euler angles of the platform about its x, y and z axis are represented by ϕ, θ and ψ, respectively. The corresponding discrete-time measurement model at the k^{th} sampling instant can be summarized as

$$\mathbf{z}_{f_k} = \mathbf{h}_k(\mathbf{x}_k) + \mathbf{v}_k, \tag{30}$$

where $\mathbf{v}_k$ is the associated sensor noise, whose covariance is represented by $\mathbf{V}_k \in \mathbf{R}^{6\times 6}$. Note that the chosen selection of sensor measurements ensures the observability of all the system states estimated by the designed EKF. The calculation of the optimal Kalman gain $\mathbf{K}$ and the correction step for the system states and error covariance are summarized as

$$\mathbf{K}_k = \mathbf{P}_{k|k-1}\mathbf{H}_k^T\left(\mathbf{H}_k\mathbf{P}_{k|k-1}\mathbf{H}_k^T + \mathbf{V}_k\right)^{-1} \tag{31a}$$

$$\hat{\mathbf{x}}(k|k) = \hat{\mathbf{x}}(k|k-1) + \boldsymbol{\lambda}_i\mathbf{K}_k(\mathbf{z}_{f_k} - \mathbf{h}(\hat{\mathbf{x}}_{k|k-1})) \tag{31b}$$

$$\mathbf{P}_k = (\mathbf{I} - \mathbf{K}_k\mathbf{H}_k)\mathbf{P}(k|k-1), \tag{31c}$$

IEEE Transactions on Automation Science and Engineering (T-ASE) paper, presented at ICRA 2026, Vienna, Austria.

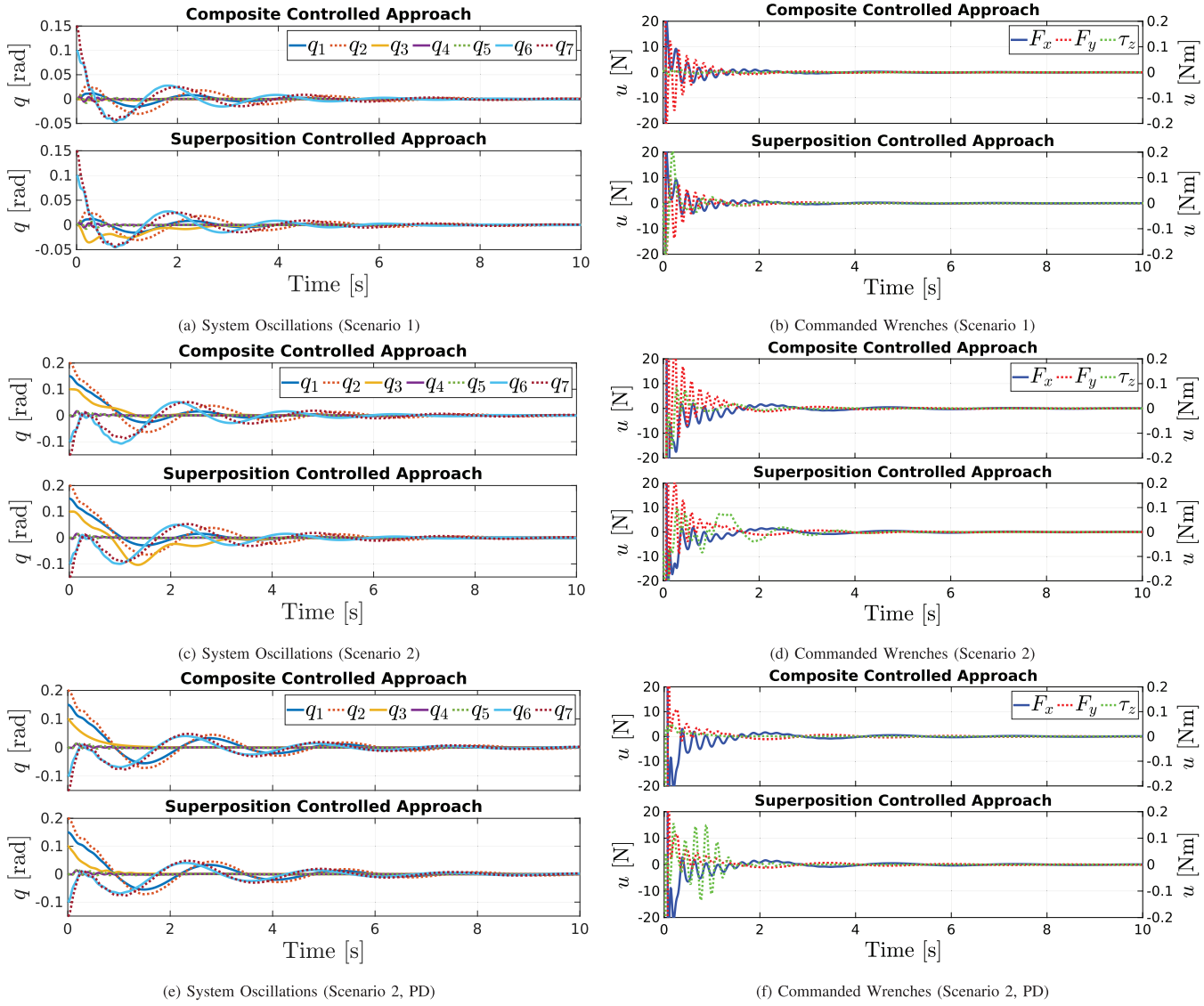

(a) System Oscillations (Scenario 1)

(b) Commanded Wrenches (Scenario 1)

(c) System Oscillations (Scenario 2)

(d) Commanded Wrenches (Scenario 2)

(e) System Oscillations (Scenario 2, PD)

(f) Commanded Wrenches (Scenario 2, PD)

Fig. 6. Oscillations of the suspended platform with the attached load, and the applied wrenches for the different scenarios.

where $\mathbf{H}_k \in \mathbf{R}^{6\times 11}$ is the state jacobian of the $\mathbf{h}(\mathbf{x})$ at the k^{th} sampling instant. The variable λ_i is considered as one if a new sensor measurement is received, or zero otherwise.

Next, we design a complementary filter using the MPU-9250 inertial measurement unit (IMU) attached to the load to measure its states q_6 and q_7. A second-order low-pass filter with a cut-off frequency of 50 Hz is utilized to reduce the noise of the IMU sensor. The sensor boards used for the estimation algorithms are summarized in Fig. 5. Note that the complementary filter is designed instead of augmenting the existing EKF with the states of the attached load, due to the memory limitations of the flight controller unit (FCU), which will be addressed in our future work. Moreover, we also observe that the dynamic coupling terms of the suspended load have minimal influence on the platform used in our experimental setup.

The measurements $\mathbf{z}_i$ obtained from the IMU are

$$\mathbf{z}_i = \begin{bmatrix} a_x & a_y & a_z & \omega_x & \omega_y \end{bmatrix}^T, \tag{32}$$

where a_x, a_y and a_z are the translational acceleration of the load along its x, y and z axis, respectively. ω_x and ω_y are the angular velocities of the attached load about its x and y axis, respectively. The estimation of the load angles q_6 and q_7 is thus obtained using the complementary filter as

$$\begin{aligned} q_6 &= \alpha \tan^{-1}(a_y/a_z) + (1-\alpha)\int \omega_x dt \\ q_7 &= \alpha \tan^{-1}(a_x/a_z) + (1-\alpha)\int \omega_y dt, \end{aligned} \tag{33}$$

where α is chosen as 0.4, ensuring a good trade-off between the high-frequency and low-frequency information, obtained from the gyroscope and the accelerometer, respectively.

V. Simulation Results

In this section, we present the results obtained in the simulations using MATLAB/Simulink, to validate our proposed control approaches. We tested our control approaches for the suspended aerial platform with the attached load

IEEE Transactions on Automation Science and Engineering (T-ASE) paper, presented at ICRA 2026, Vienna, Austria.

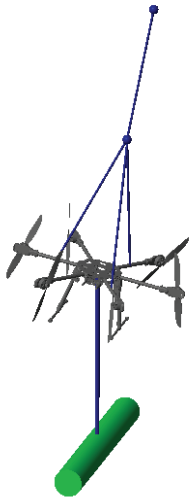

Fig. 7. Stabilization of the suspended multirotor platform with the attached load about a non-zero equilibrium point.

Fig. 8. Simulated omnidirectional multirotor platform suspended using cables.

in two different scenarios. In the first scenario, the complete system is stabilized from initial perturbations applied only to the attached load, while in the second scenario, the whole system is stabilized from an initial orientation given to both the suspended platform and the attached load. We then present the results of our robustness analysis in this section.

A. Simulation Setup

The parameters of the simulated system are chosen to be the same as the actual system. For instance, the mass of the suspended platform is found to be 4.06 kg. The principal inertia of the platform along the x, y and z axis are 0.0646, 0.0646, and 0.0682 kg□m, respectively. The length of each of the three cable links L_1, L_2, and L_3 is 0.75 m. The experiments mentioned in this work are conducted in an indoor environment. However, for the envisioned target application with a crane system (Fig. 1), the length of L_1 will be much greater than L_2. The mass of the cables with length L_1, L_2 and L_3 are 0.15 kg, 0.32 kg and 0.1 kg, respectively, while the attached slung load weighs 1.4 kg. All the simulations in our analysis are implemented at a sampling frequency of 1000 Hz.

B. Stabilization of the Complete System

We next analyze the stabilization of the suspended platform with the attached load. The oscillation angles, along with the applied wrenches for both scenarios, are shown in Fig. 6. The initial perturbations for the two scenarios are summarized in Table I. The control gains are chosen the same for both the approaches utilizing feedback linearization, which are $\hat{\mathbf{K}}_{ps} = \overline{\mathbf{K}}_{ps} = \text{diag}(300, 300, 50)$, $\hat{\mathbf{K}}_{pm} = \overline{\mathbf{K}}_{pm} = \text{diag}(3500, 3500)$, $\hat{\mathbf{K}}_{pf} = \overline{\mathbf{K}}_{pf} = \text{diag}(1000, 1000)$, $\hat{\mathbf{K}}_{ds} = \overline{\mathbf{K}}_{ds} = \text{diag}(250, 250, 20)$, $\hat{\mathbf{K}}_{dm} = \overline{\mathbf{K}}_{dm} = \text{diag}(500, 500)$ and $\hat{\mathbf{K}}_{df} = \overline{\mathbf{K}}_{df} = \text{diag}(100, 100)$. We have utilized the same control gains for both scenarios. Additionally, to analyze the performance of the proposed approach, we evaluate three key performance indicators (KPIs), which are the response time, peak response, and energy efficiency to evaluate the control approaches, as summarized in Table II. We define the response time as the time taken to reach the steady state within 1% of its final equilibrium state. The peak response in Table II is the absolute maximum overshoot observed during the transient response. Finally, energy consumption is a measure obtained similar to [36], and is dependent on both the commanded PWM pulse and thrust generated by each propulsion unit. The energy consumption metric $\hat{E}$ is calculated as

$$\hat{E} = \sum \left(\sum_{i=1}^{N} F_{m_i}.\omega_i \right) \Delta t, \tag{34}$$

where F_{m_i} is the force exerted by the i^{th} thruster unit and N is the number of actuation units, being 6 and 8 for the underactuated aerial platform and omnidirectional platform, respectively. Note that we show the KPIs for only the joints corresponding to the attached load, which are q_6 and q_7.

The system oscillations for the two scenarios 1 and 2 are plotted in figures 6a and 6c, respectively, with their corresponding commanded wrenches being plotted in Fig 6b and 6d, respectively. It is observed that the initial perturbations given to both the suspended platform and the attached load have more impact on the complete system, as compared to the initial perturbations given only to the attached load.

TABLE I

INITIAL PERTURBATIONS OF THE SUSPENDED PLATFORM AND THE ATTACHED LOAD FOR THE DIFFERENT VALIDATION SCENARIOS. THE PERTURBATION ANGLES ARE MEASURED IN RADIANS

	q_1	q_2	q_3	q_4	q_5	q_6	q_7
Scenario 1	0	0	0	0	0	0.1	0.15
Scenario 2	0.15	0.2	0.1	0	0	-0.1	-0.15

TABLE II

KEY PERFORMANCE INDICATORS (KPIS), WITH CA AND SA DENOTING COMPOSITE APPROACH AND SUPERPOSITION APPROACH, RESPECTIVELY

	Response Time (s)		Peak Response (rad)		Energy Consumption Metric
	q_6	q_7	q_6	q_7	
S1 (CA)	7.44	9.69	0.047	0.043	21870
S1 (SA)	7.49	9.69	0.045	0.043	20640
S2 (CA)	8.84	11.39	0.107	0.086	31560
S2 (SA)	8.84	11.40	0.099	0.092	29610
S2 (CA, PD)	11.43	12.98	0.069	0.076	29060
S2 (SA, PD)	11.40	12.93	0.069	0.076	29470

IEEE Transactions on Automation Science and Engineering (T-ASE) paper, presented at ICRA 2026, Vienna, Austria.

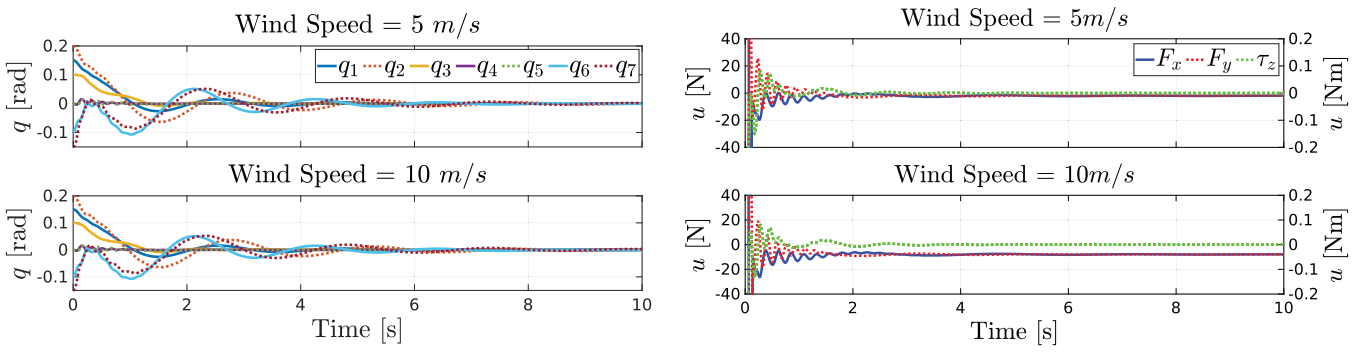

(a) System Oscillations (b) Commanded Wrenches

Fig. 9. Numerical robustness test of the composite controller with different wind disturbances of speed $5m/s$ and $10m/s$.

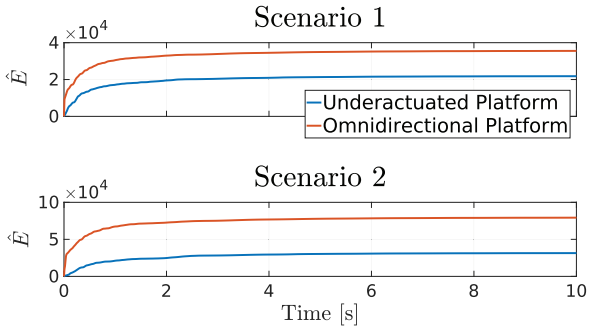

Fig. 10. Energy comparison of the omnidirectional and underactuated aerial platforms for scenarios 1 and 2.

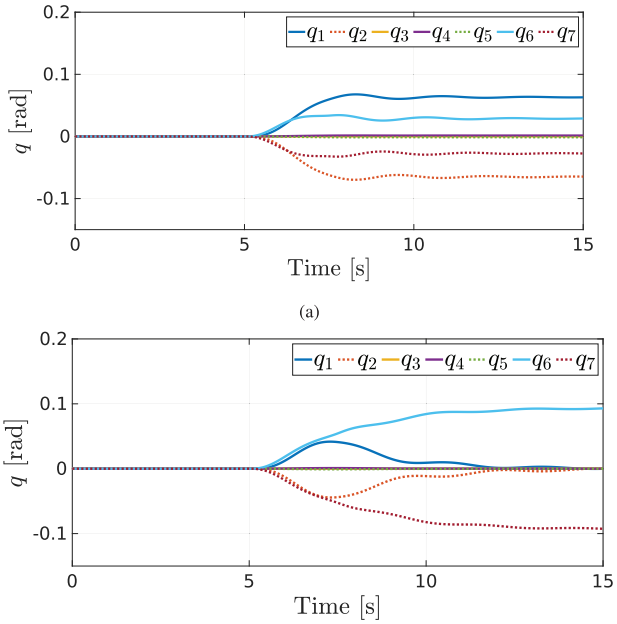

(a)

(b)

Fig. 11. System behaviour under the influence of the wind (a) without integral action and (b) with integral action. The wind disturbance is applied from 5 s.

We also observe that by utilizing the same control gains, the proposed superposition approach is slightly more energy efficient than the designed composite controller. Additionally, we observe that the peak response during the stabilization of q_6 is slightly higher for the composite control approach, while the superposition approach has a higher peak response for the joint q_7. For scenario 1, the commanded wrench F_y is observed to have an oscillation transient of higher amplitude for the composite approach as compared to the proposed superposition approach. A similar observation can also be made for scenario 2 (Fig 6d). A possible explanation for such an observation is that the separation between the different time-scale dynamics is not large enough, due to which the assumed equilibrium conditions for the slow and medium-fast dynamics controller are only partially valid, which is not the case with the superposition approach. As a result, the undesired forces induced by the interaction between these dynamics need to be further compensated to ensure the stability of the complete system.

In order to reduce the effects of modeling errors on the designed control approaches, we analyze the PD controller for the slow dynamics, together with the feedback linearization for the other dynamics. This analysis is shown only for the scenario 2, and it is observed from Fig. 6e, that the stabilization response has a reduced peak when compared with the previous response. This effect is more significant for the composite controlled approach than the superposition controlled approach, as utilizing comparatively less system dynamics reduces the effect of the equilibrium assumption, which was done previously. Note that the control coefficient for the slow dynamics control is chosen differently, as the effective gains [42] of the controller have now changed. We additionally choose different gains for medium-fast system dynamics to obtain a desired system response. The gains are chosen as $\hat{\mathbf{K}}_{ps} = \overline{\mathbf{K}}_{ps} = \text{diag}(3500, 3500, 50)$, $\hat{\mathbf{K}}_{pm} = \overline{\mathbf{K}}_{pm} = \text{diag}(3000, 3000)$, $\hat{\mathbf{K}}_{ds} = \overline{\mathbf{K}}_{ds} = \text{diag}(3000, 3000, 20)$ and $\hat{\mathbf{K}}_{dm} = \overline{\mathbf{K}}_{dm} = \text{diag}(100, 100)$. The gains for the fast dynamics controller are kept the same, as it did not have a significant impact due to a change in the control law of the slow dynamics. From Fig. 6e and 6f, we can thus conclude that the response from the composite control approach has improved significantly in comparison to improvements in the superposition approach, after incorporating the PD controller for the slow dynamics. Note that the attached supplementary video further provides two additional scenarios for more comparison.

IEEE Transactions on Automation Science and Engineering (T-ASE) paper, presented at ICRA 2026, Vienna, Austria.

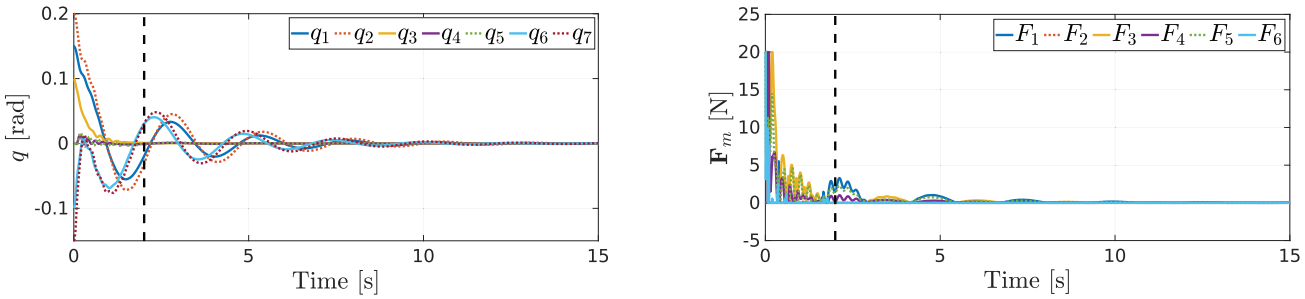

(a) System Oscillations (b) Actuator Forces

Fig. 12. System response and actuator forces during stabilization, in the presence of failure of motor numbers 2 and 6. The rotor failure happens at 2 s, marked by the black dashed line.

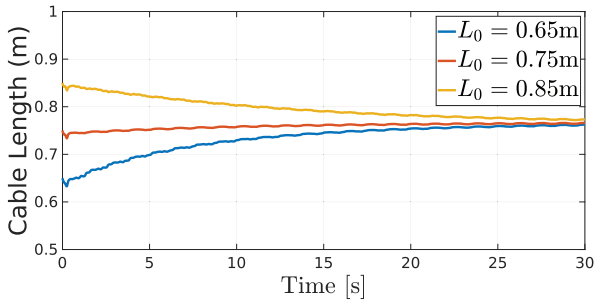

Fig. 13. Estimation of cable length from different initial conditions.

TABLE III
KEY PERFORMANCE INDICATORS (KPIS) FOR OMNIDIRECTIONAL AERIAL PLATFORM USING COMPOSITE CONTROL APPROACH

	Response Time (s)		Peak Response (rad)		Energy Consumption Metric
	q_6	q_7	q_6	q_7	
S1 (CA)	7.45	9.66	0.045	0.041	35630
S2 (CA)	8.83	11.38	0.109	0.082	79470

C. Stabilization About Non-Zero Equilibrium Points

The attached load, in our case, cannot be directly actuated and is rather stabilized using the coupled dynamics of the suspended platform. Additionally, the suspended platform utilized in this work is underactuated, and therefore it can only exert a 3 DoF wrench for its 7 DoF dynamics consisting of the states $\mathbf{q}_s$, $\mathbf{q}_f$, and $\mathbf{q}_m$. As a result, the system does not satisfy the rank condition for full controllability, meaning it cannot be driven to an arbitrary state through the available control inputs. However, the system remains stabilizable, as the control inputs can influence and regulate the unstable modes, ensuring that the system can reach and maintain a desired equilibrium despite its actuation constraints. Therefore, in this work, we considered the stabilization of the complete system only at its equilibrium of zero. However, zero is not the only stable equilibrium of the system, for instance, $q_1 = 0, q_2 = 0.19, q_3 = 0, q_4 = 0$, $q_5 = 0.01, q_6 = 0$ and $q_7 = -0.20$ radians can be considered as an equilibrium point and Fig. 7 depicts the stabilization of the complete system about this non-zero equilibria. Note that its stabilization about any possible set is not possible, as the underactuation of the suspended platform allows statically only a limited set of equilibrium points.

D. Comparision With Omnidirectional Platform

In this section, we evaluate the performance and the energy consumption of the underactuated planar thrust platform with the omnidirectional platform. An omnidirectional platform [43] is capable of generating a 6 DoF wrench in any direction, unlike the underactuated platform. The wrench space comprises the translation forces along its x, y, and z axes, and also the rotational torques about its x, y, and z axes. Such a platform requires a minimum of 7 unidirectional actuation units [44] or 6 bidirectional actuation units [45]. The SAM platform [6] developed at DLR rather uses 8 motors installed at certain angles. This angle is obtained by solving an optimization problem that ensures a balanced wrench distribution between the different actuators while having a symmetric design. In this work, we utilize the allocation matrix of SAM after scaling it down to the same size as that of our underactuated platform, as shown in Fig. 8. The modified allocation matrix $\mathbf{A}_o$ of the omnidirectional platform can be summarized as

$$\mathbf{A}_o = \begin{bmatrix} 0.56 & -0.56 & 0.60 & 0.17 & -0.17 & -0.3 \\ -0.81 & 0 & 0.59 & 0.23 & 0 & 0.3 \\ -0.56 & -0.56 & -0.60 & -0.17 & -0.17 & 0.3 \\ 0 & 0.81 & -0.59 & 0 & -0.23 & -0.3 \\ -0.56 & 0.56 & 0.60 & -0.17 & 0.17 & -0.3 \\ 0.81 & 0 & 0.59 & -0.23 & 0 & 0.3 \\ 0.56 & 0.56 & -0.60 & 0.17 & 0.17 & 0.3 \\ 0 & -0.81 & -0.59 & 0 & 0.23 & -0.3 \end{bmatrix}^T \tag{35}$$

We evaluate the developed composite controller with the feedback linearization approach for the two platforms. Due to the additional wrench space of the onmidirectional platform, the controllers developed in (13), (15) and (16) will no longer be applicable to the inversion of the control effective matrices $\boldsymbol{\lambda}_s$, $\boldsymbol{\lambda}_m$ and $\boldsymbol{\lambda}_f$. Therefore, we utilize the same 3D wrench space for the omnidirectional platform as utilized by the underactuated platforms. Additionally, this will ensure a fair and equal comparison of the two platforms while using the same control gains for both of them.

The KPIs for the omnidirectional platform are highlighted in the Table. III. We observe that the response time and the peak response of both the underactuated and omnidirectional platforms are nearly identical. However, the energy consumed

IEEE Transactions on Automation Science and Engineering (T-ASE) paper, presented at ICRA 2026, Vienna, Austria.

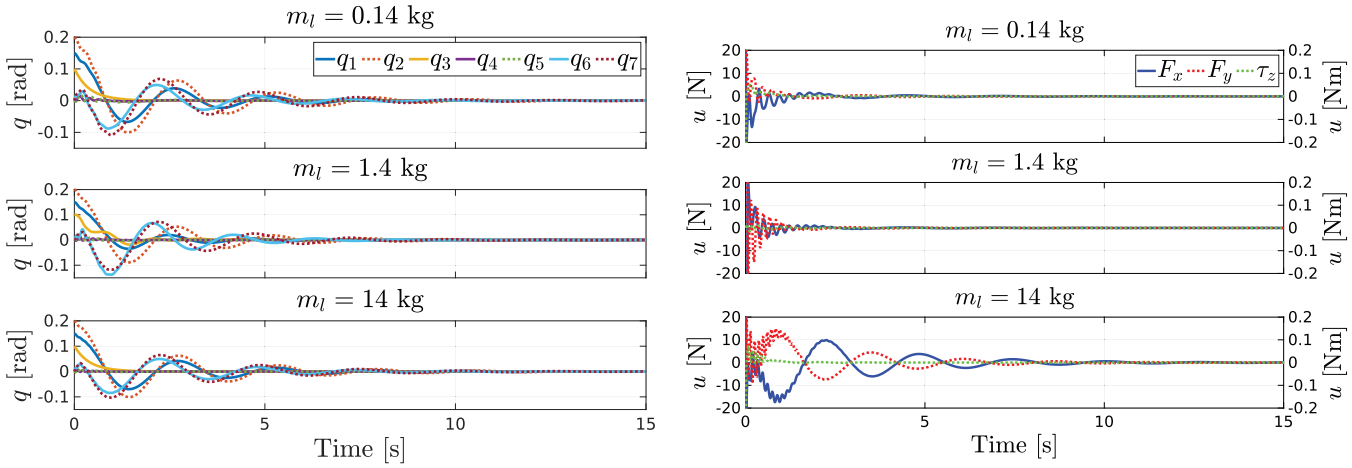

(a) System Oscillations (b) Commanded Wrenches

Fig. 14. Numerical robustness test of the composite controller with different attached loads of mass m_l = 0.14 kg, 1.4 kg and 14 kg.

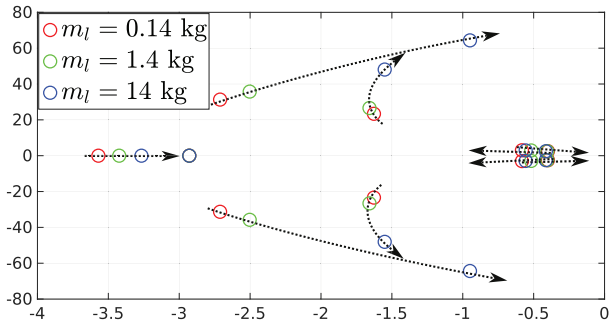

Fig. 15. Eigenvalue analysis corresponding to the robustness test in Fig. 14. The plot only shows eigenvalues close to the imaginary axis, with the arrow showing the direction of their shift. The x axis denotes the real part, while the y axis denotes the imaginary part of the computed eigenvalue.

by the omnidirectional platform is higher than the underactuated platform, by 17.19 % and 151.8 % for scenarios 1 and 2, respectively. The energy consumption metric is plotted in Fig. 10. Thus, our analysis indicates that the underactuated aerial platform is better suited than the omnidirectional platform for stabilizing the load in our chosen application.

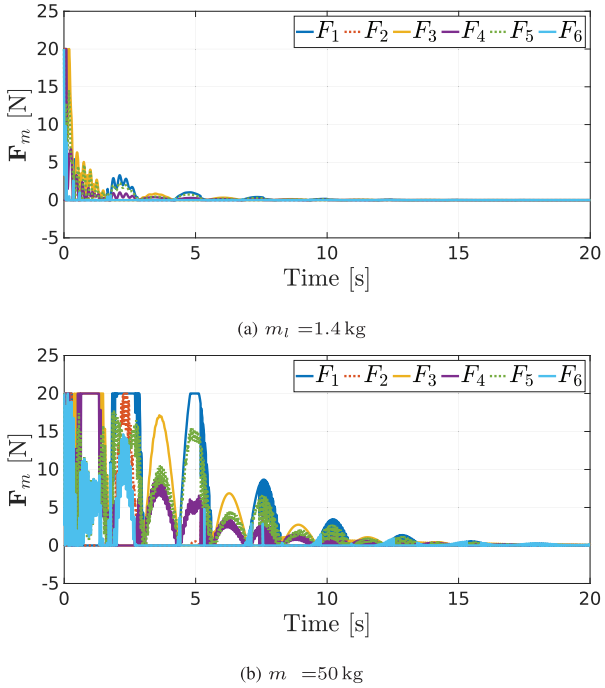

(a) m_l =1.4 kg

(b) m =50 kg

Fig. 16. Actuator forces necessary to stabilize two different attached loads of mass 1.4 kg and 50 kg.

E. Robustness and Stability Analysis

In this subsection, we analyze the robustness and stability of the composite control approach. First, we perform a robustness analysis of our proposed approach to varying wind disturbances. We consider the wind speeds of 5 m/s and 10 m/s for this analysis, which are approximately 10 knots and 20 knots, respectively. A wind speed of 10 knots is considered to be a moderate breeze, with 20 knots wind speed being a strong breeze. We assume that the wind impacts only the suspended multirotor platform along both its x axis and y axis and thus produces an external force of 3.8 N and 7.9 N for the two respective cases along both axes. As seen from Fig. 9, our approach is very robust in handling such disturbances with similar time-domain specifications for both system responses. However, we observe that the commanded wrenches (Fig. 9b) converge to a non-zero steady-state offset in order to counteract the constant external disturbance. The offsets along both the commanded x and y axis forces are 3.8 N and 7.9 N, respectively, corresponding to moderate and strong breeze conditions. These values are equivalent to the wind load exerted in each case.

To further analyze the robustness of our control approach and in order to test its applicability to outdoor scenarios, we subsequently considered the wind to impact both the suspended platform and the attached load of mass 5 kg. The wind disturbance is applied starting at 5 s, increases linearly to an amplitude of 5 N over a duration of 2.5 s, and remains

IEEE Transactions on Automation Science and Engineering (T-ASE) paper, presented at ICRA 2026, Vienna, Austria.

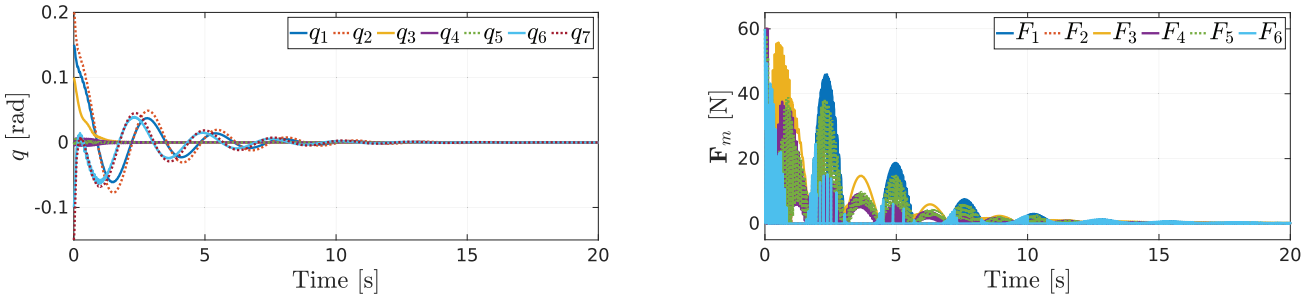

(a) System Oscillations (b) Actuator Forces

Fig. 17. System response and actuator forces with increased actuator limits, for stabilizing the attached load of mass 50 kg.

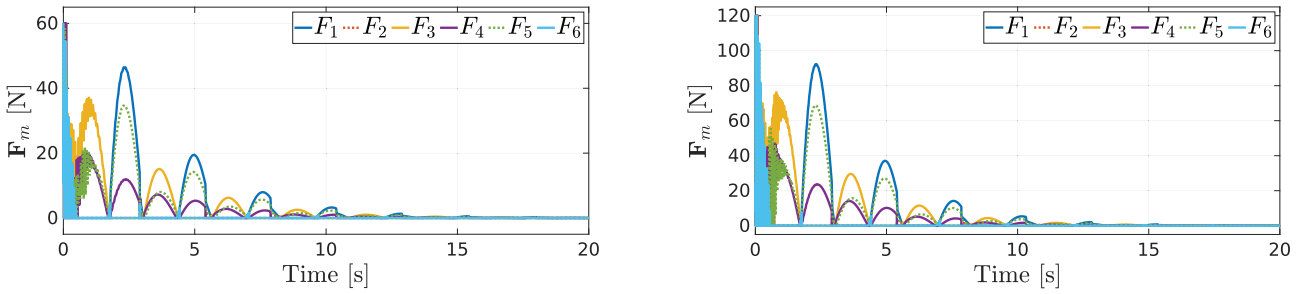

(a) m_l =50 kg (b) m_l =100 kg

Fig. 18. Actuator forces for stabilizing 50 kg and 100 kg loads with tuned gains.

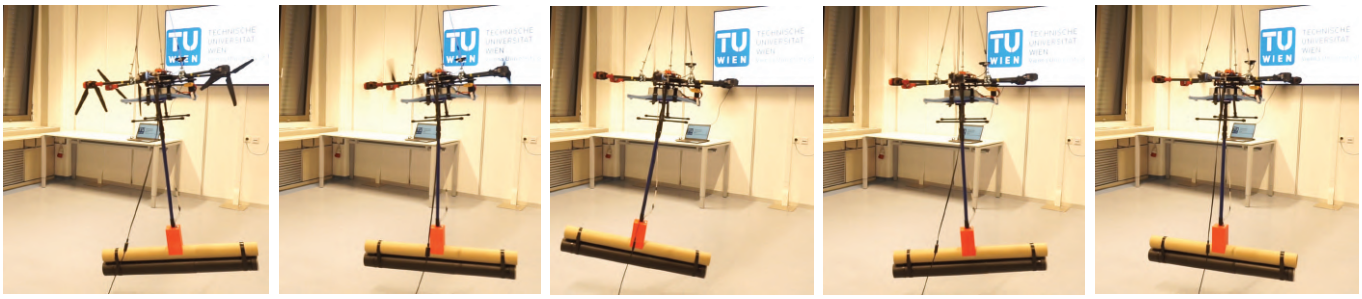

Fig. 19. Sequence of the experiments for stabilizing the suspended aerial platform with the attached unknown load using the composite control approach.

constant thereafter. We observe from Fig. 11a that under the influence of this external wind, our proposed controller can stabilize the complete system, however, a steady state error is observed across all the states, except for the joints q_3, as the wind impacts only along the x and y axis. The influence of the wind thus shifts the stable equilibrium point, which is a function of both the payload mass and the wind forces. In order to eliminate these steady-state errors, we augmented our control law with integral action as follows

$$\hat{\mathbf{u}}_s = \hat{\mathbf{J}}_s^{-T}\left(\hat{\mathbf{K}}_{ds}\dot{\tilde{\mathbf{q}}}_s + \hat{\mathbf{K}}_{ps}\tilde{\mathbf{q}}_s + \hat{\mathbf{K}}_{is}\int \tilde{\mathbf{q}}_s dt\right) \tag{36}$$

where $\hat{\mathbf{K}}_{is}$ is the integral gain. Note that the integral action is not incorporated into the medium-fast dynamics of the attached load since this subsystem cannot be stabilized around its zero equilibrium under external wind disturbances due to the absence of direct actuation. In contrast, applying integral action to the slow dynamics mitigates steady-state error resulting from external disturbances, as shown in Fig. 11b. The integral action is also not incorporated into the fast dynamics of the load, as its corresponding steady-state error is insignificant in our case. It can be inferred that under the influence of wind disturbances, the stable equilibrium of the complete system shifts, which can be directly calculated using an external wrench observer [46]. We additionally observe that due to the integral action, the relative error between the load and platform state has increased, as compared to the controller without the integral action.

Next, we demonstrate the robustness of the state-estimator to varying initial guesses of the cable length. As observed from Fig. 13, the estimated cable length from the EKF is robust to varying initial guesses L_0 = 0.65 m, 0.75 m and 0.85 m of the cable length, while converging to the actual cable length of 0.75 m. We observe that varying the covariance matrix leads to a trade-off between the rate of convergence and the accuracy of the convergence of the rope length. Note that for

IEEE Transactions on Automation Science and Engineering (T-ASE) paper, presented at ICRA 2026, Vienna, Austria.

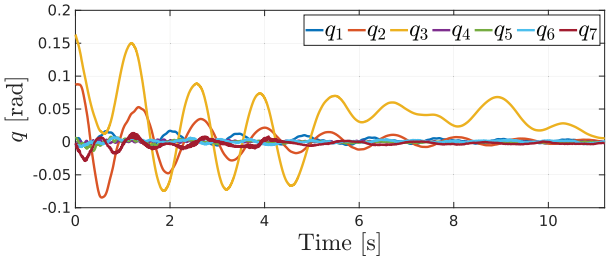

(a) Nominal Case

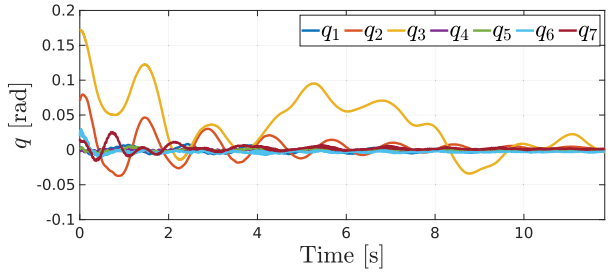

(b) Robust Case

Fig. 20. Experimental results showing oscillations angles of the platform with the attached (a) known load and (b) unknown load.

the envisioned outdoor application with cranes, the length of the first cable will be much bigger than 0.75 m, which will be analyzed in future work. The estimation of the other states related to the platform oscillations has not been analyzed in this paper and can be found in [36].

We have also tested the robustness of our approach to possible rotor failures of the planar thrust suspended aerial platform. This platform consists of six unidirectional rotors and is capable of generating a 3 DoF wrench, and therefore has a redundancy of two rotors [36]. For instance, we determine from the allocation matrix (8) that if the first motor fails, then the platform still generates the 3 DoF wrench. Similarly, if both the first and third motors fail, then the platform can still generate a wrench to span the complete 3D space. However, we observe that if the first and second motor fail simultaneously, then the platform can no longer generate the force F_x along its positive x axis, which can be one of the limitations of this platform, although it provides redundancy with respect to other motor failures and its various possible combinations. Fig. 12 illustrates the applied wrench in the presence of two motor failures occurring at 2 s from the start of the simulation, showing that the stabilization performance remains unaffected. This is attributed to the redistribution of motor wrenches achieved through the optimization solution of (10).

Next, we analyze the robustness of the composite control approach to varying attached loads. The nominal weight of the attached load for the simulation study is considered as 1.4 kg. For the robustness study, we vary the attached load by ten times its nominal weight and evaluate the controller. This variation will not be considered by the controller, which relies only on the nominal mass. From Fig. 14, we observe that the nominal controller is successful in handling the unknown attached load and subsequently stabilizes the complete system with a comparable response time to the nominal system response. However, the demanded control wrench for the system with an attached load of $m_l = 14$ kg is significantly higher, as compared to the other configurations. Note that the robustness analysis is performed using the feedback linearization-based controller, due to its increased dependency on the model parameters.

We also performed local stability analysis near the equilibrium, by analyzing the eigenvalues of the closed-loop system dynamics, obtained by equating the control commands (13), (15), and (16) in the system dynamics (1). The eigenvalues close to the imaginary axis are plotted in Fig. 15. We observe that the eigenvalues for all the different cases are negative. Additionally, we also observe that increasing the mass of the attached load shifts most of the eigenvalues towards the imaginary axis because it becomes more difficult for the nominal control to stabilize the unknown mass. For our test-case scenarios, we observe that increasing the mass of the attached load up to 40 kg results in comparable time-domain characteristics, while increasing it further leads to increased high-frequency oscillations of the complete system during the stabilization.

F. Scalability Analysis

In this section, we analyze the scalability of the suspended aerial platform necessary for the stabilization of comparatively larger payloads. In our previous case, we consider the payload to be of mass 1.4 kg for the nominal case (Fig. 6), while it is increased ten times to 14 kg for the robustness analysis (Fig. 14). We observe that in both these scenarios, the maximum applied force from its actuation units is below its saturation limits of 20 N. However, in an overhead crane system, the maximum mass of the attached payload can be significantly larger, requiring a corresponding increase in propulsion force from the suspended platform to effectively stabilize the attached load.

To analyze the scaling of the platform for larger payloads, we first determine the propulsion force needed to stabilize an attached load 50 times greater than the nominal mass. For a 50 kg load, as shown in Fig. 16, the actuators saturate, unlike for the 1.4 kg nominal load. This results in a marginal increase in the response time and peak response due to actuator saturation. To mitigate this, we increase the maximum actuator force to 60 N for the 50 kg payload, and, as shown in Fig. 17, the system response closely matches the nominal response. Similarly, for a 100 kg payload, a saturation limit of 120 N is required. These increases in saturation limits follow a relationship with the payload mass. It is important to note that the saturation limits also depend on operating conditions, such as wind disturbances or any involved aggressive maneuvers. Additionally, higher thrust requirements call for larger propulsion systems, such as the SAM system [6], which uses 16-inch propellers driven by brushless DC motors capable of generating thrusts of up to 150 N.

G. Gain Tuning Strategy

In this section, we propose a gain-tuning strategy to improve controller performance under varying load conditions. As seen in Fig. 16, using the same controller gains for both

IEEE Transactions on Automation Science and Engineering (T-ASE) paper, presented at ICRA 2026, Vienna, Austria.

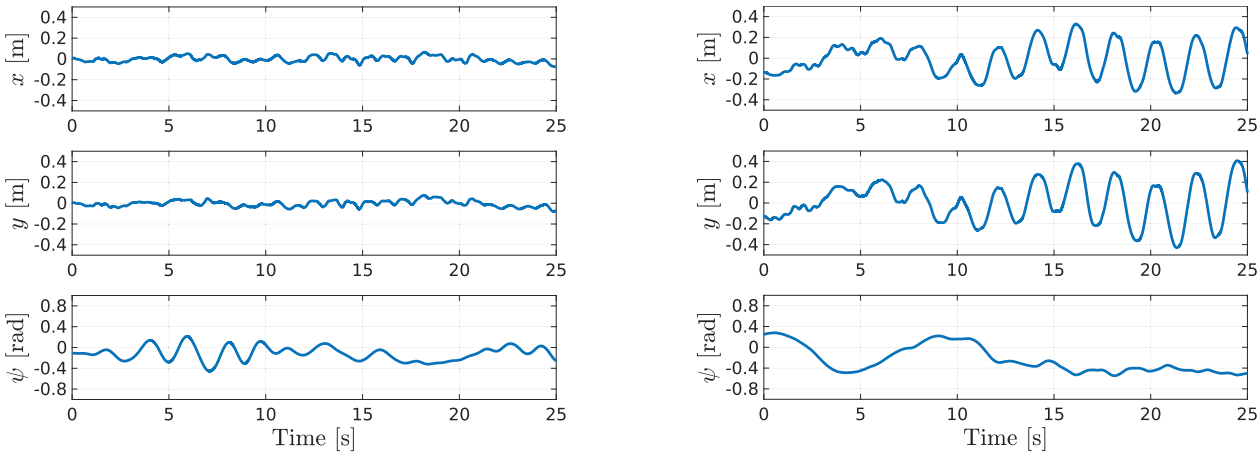

(a) Controlled Case (b) Uncontrolled Case

Fig. 21. Operational space coordinates during the stabilization experiments with the overhead crane setup.

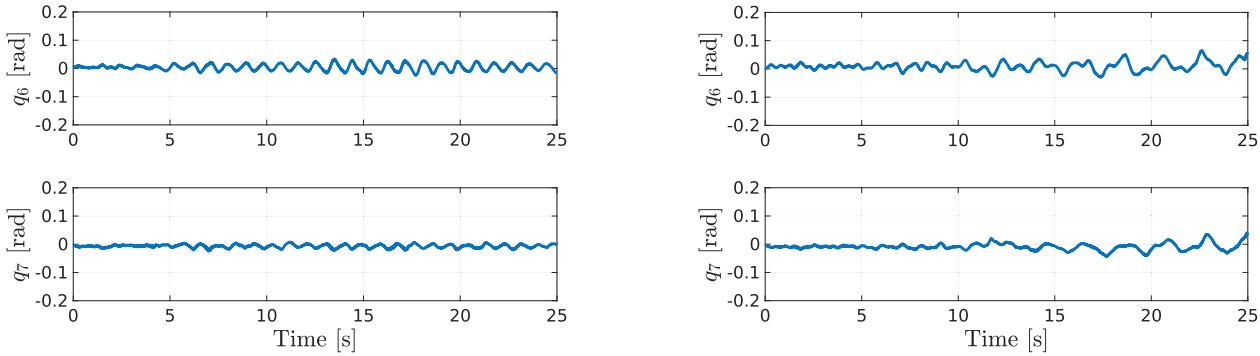

(a) Controlled Case (b) Uncontrolled Case

Fig. 22. States of the attached load during stabilization experiments with the overhead crane setup.

50 kg and 1.4 kg load leads to high-frequency control effort, characterized by rapid switching behavior of the control input. This suggests that the region of attraction of the closed-loop controlled system shrinks with increasing load mass, highlighting the need for load-dependent gain tuning. To address this, we increase the proportional and derivative gains based on the attached load mass. For instance, for stabilizing a 50 kg payload, the proportional and derivative gains are increased to $\overline{\mathbf{K}}_{ps} = \text{diag}(12162, 12162, 174)$, $\overline{\mathbf{K}}_{pm} = \text{diag}(10424, 10424)$, $\overline{\mathbf{K}}_{pf} = \text{diag}(3474, 3474)$, $\overline{\mathbf{K}}_{ds} = \text{diag}(9744, 9744, 651)$, $\overline{\mathbf{K}}_{dm} = \text{diag}(324, 324)$ and $\overline{\mathbf{K}}_{df} = \text{diag}(324, 324)$. The gain-tuning strategy is demonstrated using the superposition control approach, although it is also applicable to the composite controller. The stabilization results, shown in Fig. 18, reveal that the actuation force from the platform exhibits a lower frequency content compared to the scenario without gain tuning (Fig. 17b).

VI. Experimental Validation

The experiments are conducted using the planar-thrust suspended platform [36], as shown in Fig. 1. The propulsion system of the platform consists of six brushless DC motors each with a rating of 380 KV, fitted with a 15-inch propeller, and each of these units is capable of generating up to 20 N thrust at maximum throttle. The Pixhawk Cube Orange is used as the flight controller unit (FCU), which is responsible for running both the state-estimation and controller modules. Prior to integrating the onboard sensors in the state estimation framework, a detailed calibration procedure is carried out to ensure accurate and drift-free sensor measurements. The calibration is performed using the standard procedures provided by the PX4 autopilot stack through the QGroundcontrol interface. This process involves placing the platform in six different orientations for accelerometer calibration, rotating it along specific axes for compass calibration, and keeping the vehicle stationary for gyroscope calibration. Additionally, the proposed control framework also leverages the PX4 firmware using the Simulink Support Package to enable real-time implementation and online parameter tuning at a frequency of around 500 Hz.

We have validated our proposed approach in two distinct lab setups. The first involves an indoor setup with a fixed suspension point, while the second utilizes an overhead crane system to emulate more realistic operational conditions. The cables used for the suspension of both the platform and the attached load in the first setup are made of silver-galvanized steel with a tensile strength of 1960 N/mm^2. In the overhead crane setup, the load-bearing cables are steel wire ropes regularly maintained and inspected according to DIN 15020 and DIN

IEEE Transactions on Automation Science and Engineering (T-ASE) paper, presented at ICRA 2026, Vienna, Austria.

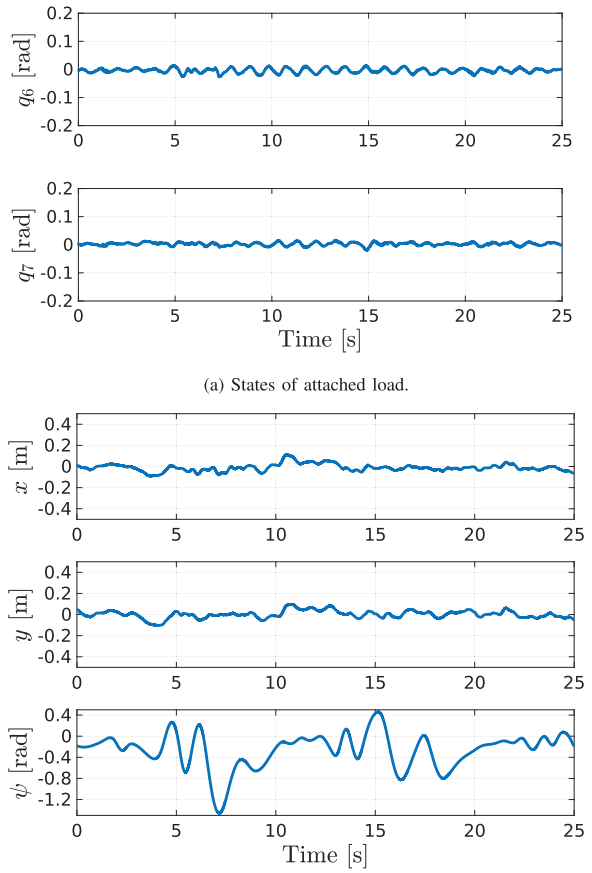

(a) States of attached load.

(b) States of the platform.

Fig. 23. States of the complete system during stabilization experiments with the overhead crane setup, in the presence of rotor failure.

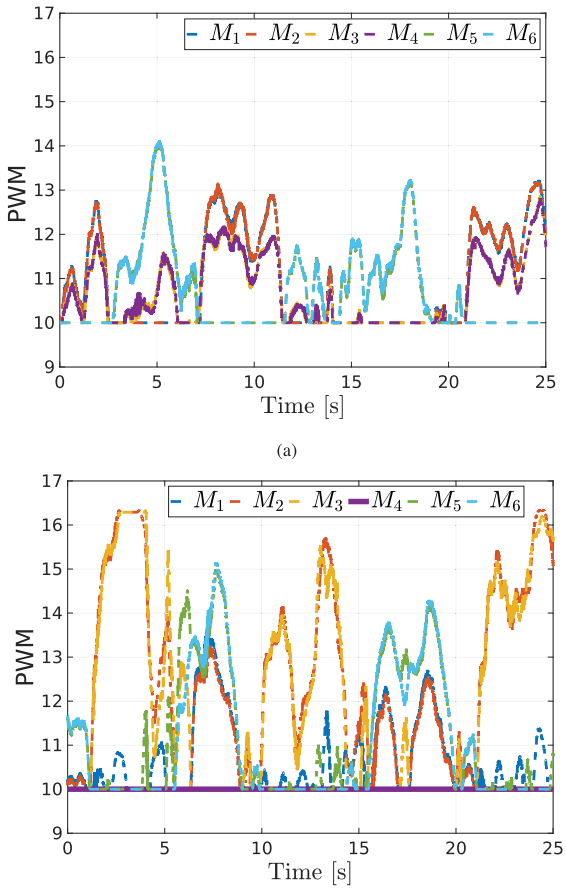

(a)

(b)

Fig. 24. Motor inputs for the (a) nominal case with six functional rotors and (b) rotor-failure case where the motor M4 is non-functional.

13414-1, ensuring compliance with industrial safety standards. The overhead crane is equipped with a variable frequency drive (VFD) system, enabling the operator to manually control the hoisting (up/down), trolley (left/right), and bridge travel (forward/backward) motions.

A. Indoor Lab Setup With Fixed Suspension

The experimental results for the suspended platform with the attached load are shown in Fig. 20a. We discuss the scenario 2, as its perturbation condition is found to have a higher impact on the system than the scenario 1. Additionally, we only discuss the composite control approach utilizing PD for the slow dynamics, as the proposed superposition approach demonstrated comparable results. The feedback linearization approach for the slow dynamics is not studied in the experiments, as it demands more high-frequency control wrench than PD controller, as found in the simulation studies (Fig. 6d). The control coefficients for the suspended platform and attached load are chosen as $\overline{\mathbf{K}}_{ps} = \text{diag}(17.31, 17.31, 0.4)$, $\overline{\mathbf{K}}_{pm} = \text{diag}(5, 5)$, $\overline{\mathbf{K}}_{pf} = \text{diag}(0.1, 0.1)$, $\overline{\mathbf{K}}_{ds} = \text{diag}(12.65, 12.65, 0.2)$, $\overline{\mathbf{K}}_{dm} = \text{diag}(0.0045, 0.0045)$ and $\overline{\mathbf{K}}_{df} = \text{diag}(0.12, 0.12)$. The controller gains for the slow system are selected first, since its associated oscillations exhibit the largest amplitude and, consequently, have the most dominant effect on the overall system stabilization due to its significant wrench generation. Subsequently, the gains for the medium-fast dynamics of the attached load are determined, followed by the tuning of the fast dynamics corresponding to the second spherical joint.

The settling-time for all the states is found to be satisfactory, with a comparatively slow convergence of the joint q_3. The estimation of the joint q_3 utilizes an onboard magnetometer as an external observation in the EKF. Due to the low sampling rate of the magnetometer compared to the accelerometer and the gyroscope, the estimates of the q_3 are corrected less frequently in the EKF, as compared to the other joint angles, which will be addressed in the future with additional onboard sensors. Besides the nominal load of mass 1.4 kg, we have also conducted experiments by adding an unknown load of mass 0.45 kg. We successfully demonstrate that our proposed control approach is robust to uncertainties in the mass of the attached load (Fig. 20b). The sequence of the experiments conducted in the indoor crane setup is shown in Fig. 19. The provided supplementary video further presents an additional stabilization scenario where the attached load is subjected to an external disturbance.

The effect of different control gains on the complete system has been evaluated, which shows a trade-off between the three subsystems. For instance, a high gain for the load dynamics can make the slow dynamics of the platform converge slower

IEEE Transactions on Automation Science and Engineering (T-ASE) paper, presented at ICRA 2026, Vienna, Austria.

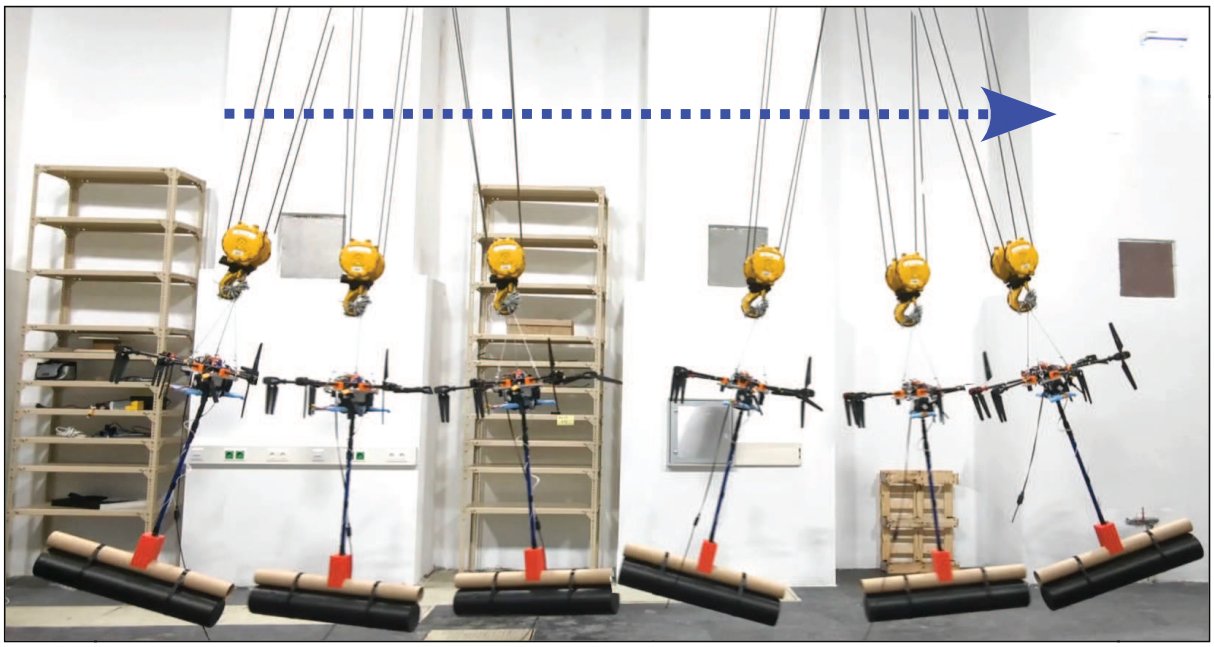

Fig. 25. Sequence of experiments with the overhead crane, demonstrating the uncontrolled case. The blue arrow depicts the direction of motion.

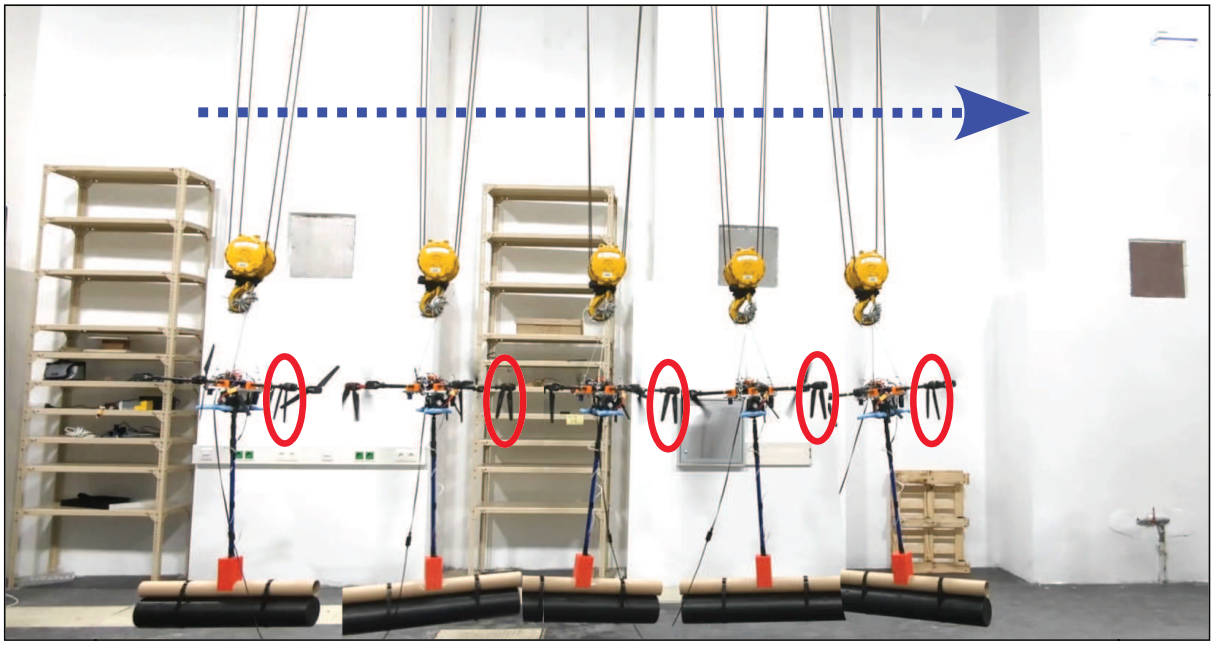

Fig. 26. Sequence of experiments with the overhead crane, for the case of rotor failure, where the red ellipse highlights the failure of rotor 6.

than the former. Similarly, a high gain for the platform, with comparatively low gains for the attached load, can induce uncontrolled oscillations when the eigenmodes of the former dominate over the other. Additionally, the z axis torque τ_z is not utilized for stabilizing the medium-fast and fast dynamics in the composite control law (17); utilizing which might lead to further reduction of the settling-time by exploiting the coupling between them. Moreover, in order to limit the control actions within half the maximum capacity of the actuators due to safety considerations, the maximum thrust generated by each actuation unit is limited to 9 N; increasing which might lead to a faster convergence.

B. Overhead Crane Setup

In this section, we present the experimental results of the stabilization performed on the overhead crane setup. The stabilization wrench is generated using the operational space controller derived in (26). The parameters of this crane setup are different from the previous case. Specifically, the length of the first cable is 3.7 m, while the second cable has a length of 0.45 m. Additionally, the suspended payload has a considerable mass of 22 kg. The control gains for the operational-space controller corresponding to the task coordinates $\mathbf{x}_o$ are chosen as $\mathbf{K}_{po} = \text{diag}(40, 40, 0.27)$ and $\mathbf{K}_{do} = \text{diag}(18, 18, 0.1)$. The gains for the load dynamics

IEEE Transactions on Automation Science and Engineering (T-ASE) paper, presented at ICRA 2026, Vienna, Austria.

$\mathbf{K}_{pl}$ and $\mathbf{K}_{dl}$ are chosen as diag(2, 2) and diag(0.002, 0.002), respectively. Furthermore, the saturation limits of the actuator thrust are increased to 75 % of its maximum capacity in this setup, compared to 50 % used in indoor laboratory experiments.

The stabilization results corresponding to the states $\mathbf{x}_o$ and $\mathbf{x}_l$ are shown in Fig. 21 and Fig. 22, respectively. The experiments are conducted for both the controlled and uncontrolled scenarios. In each case, the overhead crane is operated in a similar manner, where the operator continuously moves the system back and forth between two distinct locations at the maximum feasible speed, to enable a fair comparison of the stabilization performance. It is observed that, in the absence of control, the states x and y demonstrate an oscillatory motion, whereas, for the controlled case, these states always stay bounded between ± 0.1 m. The motion of the state ψ is irregular for the uncontrolled case but stays bounded with approximately twice the range of the corresponding controlled state. The states q_6 and q_7 demonstrate similar behavior as the states x_1 and x_2, such as their amplitude increases gradually for the uncontrolled case, while it remains bounded for the controlled case.

We have also conducted stabilization experiments in the presence of rotor failure, as shown in Fig. 26. In the previous cases, all six rotors of the suspended platform generate thrust to stabilize the platform. However, in this scenario of rotor failure, one of its actuation units is not working, and the objective is to stabilize the complete system under such circumstances. The system behavior is shown in Fig. 23, where we observe that the states x, y, q_6, and q_7 demonstrate a similar behavior as the previous controlled case (Figs. 21a and 22a). However, the state ψ exhibits increased oscillations compared to the previous case. Furthermore, as shown in Fig. 24, the remaining operational motors increase their thrust output to compensate for the failed rotor. This behavior is attributed to the redistribution of motor wrenches achieved through the optimization solution of (10). In contrast, for the nominal case, the thrust generated by all motors is relatively lower.

VII. Conclusion and Future Work

This paper presented a novel whole-body composite feedback control based on singular perturbation theory for stabilizing a suspended multirotor platform carrying a slung load. Building upon this framework, we developed a superposition approach based on shared control and compared it with the composite controller. Furthermore, to address specific scenarios where the time-scale separation between two subsystems of the triple spherical pendulum becomes negligible, we designed an operational space controller and validated it on an actual overhead crane setup. Our approaches are underactuated in nature as they generate a 3-DoF wrench in order to stabilize the 7-DoF system while relying on only onboard sensors, thus making it applicable for outdoor applications. The effectiveness of our approaches was extensively validated in different scenarios across two distinct lab settings, using both numerical simulations and experiments. Additionally, we performed a numerical stability analysis and also demonstrated that our control approach is robust to varying payloads and external wind disturbances, while effectively handling potential actuator failures of the platform.

In the future, we plan to validate our proposed approach by using a larger suspended multirotor platform capable of transporting heavy loads up to 500 kg. It would also be interesting to perform tracking tasks with the designed whole-body controller, once mounted on an active crane system. Finally, cameras can be mounted on the platform in order to improve the accuracy of the existing Kalman filter for estimating the joint angles and their velocities.

References

[1] F. Ruggiero, V. Lippiello, and A. Ollero, "Aerial manipulation: A literature review," *IEEE Robot. Autom. Lett.*, vol. 3, no. 3, pp. 1957–1964, Jul. 2018.

[2] A. Ollero, M. Tognon, A. Suarez, D. Lee, and A. Franchi, "Past, present, and future of aerial robotic manipulators," *IEEE Trans. Robot.*, vol. 38, no. 1, pp. 626–645, Feb. 2022.

[3] A. Ollero et al., "The AEROARMS project: Aerial robots with advanced manipulation capabilities for inspection and maintenance," *IEEE Robot. Autom. Mag.*, vol. 25, no. 4, pp. 12–23, Dec. 2018.

[4] N. Staub, D. Bicego, Q. Sablé, V. Arellano, S. Mishra, and A. Franchi, "Towards a flying assistant paradigm: The OTHex," in *Proc. IEEE Int. Conf. Robot. Autom. (ICRA)*, May 2018, pp. 6997–7002.

[5] K. Kondak et al., "Aerial manipulation robot composed of an autonomous helicopter and a 7 degrees of freedom industrial manipulator," in *Proc. IEEE Int. Conf. Robot. Autom. (ICRA)*, May 2014, pp. 2107–2112.

[6] Y. S. Sarkisov et al., "Development of SAM: Cable-suspended aerial manipulator," in *Proc. Int. Conf. Robot. Autom. (ICRA)*, May 2019, pp. 5323–5329.

[7] C. Gabellieri, Y. S. Sarkisov, A. Coelho, L. Pallottino, K. Kondak, and M. J. Kim, "Compliance control of a cable-suspended aerial manipulator using hierarchical control framework," in *Proc. IEEE/RSJ Int. Conf. Intell. Robots Syst. (IROS)*, Oct. 2020, pp. 7196–7202.

[8] A. Coelho et al., "Hierarchical control of redundant aerial manipulators with enhanced field of view," in *Proc. Int. Conf. Unmanned Aircr. Syst. (ICUAS)*, Jun. 2021, pp. 994–1002.

[9] A. Yigit, G. Grappe, L. Cuvillon, S. Durand, and J. Gangloff, "Preliminary study of an aerial manipulator with elastic suspension," in *Proc. IEEE Int. Conf. Robot. Autom. (ICRA)*, May 2020, pp. 4287–4293.

[10] A. Yigit, M. A. Perozo, L. Cuvillon, S. Durand, and J. Gangloff, "Improving dynamics of an aerial manipulator with elastic suspension using nonlinear model predictive control," in *Proc. IEEE Int. Conf. Robot. Autom. (ICRA)*, May 2021, pp. 533–539.

[11] A. Yigit, M. A. Perozo, L. Cuvillon, S. Durand, and J. Gangloff, "Novel omnidirectional aerial manipulator with elastic suspension: Dynamic control and experimental performance assessment," *IEEE Robot. Autom. Lett.*, vol. 6, no. 2, pp. 612–619, Apr. 2021.

[12] F. Kong, S. Monteleone, G. Grioli, M. G. Catalano, and A. Bicchi, "A robotic aerial platform with functionally anthropomorphic arms designed for physical interaction," in *Proc. IEEE/RSJ Int. Conf. Intell. Robots Syst. (IROS)*, Oct. 2022, pp. 7581–7588.

[13] F. Kong, G. Zambella, S. Monteleone, G. Grioli, M. G. Catalano, and A. Bicchi, "A suspended aerial manipulation avatar for physical interaction in unstructured environments," *IEEE Access*, vol. 12, pp. 48108–48125, 2024.

[14] J. Lee et al., "Virtual reality via object pose estimation and active learning: Realizing telepresence robots with aerial manipulation capabilities," *Field Robot.*, vol. 3, no. 1, pp. 323–367, Jan. 2023.

[15] Y. S. Sarkisov et al., "Hierarchical whole-body control of the cable-suspended aerial manipulator endowed with winch-based actuation," in *Proc. IEEE Int. Conf. Robot. Autom. (ICRA)*, May 2023, pp. 5366–5372.

[16] A. Yiğit, L. Cuvillon, M. A. Perozo, S. Durand, and J. Gangloff, "Dynamic control of a macro–mini aerial manipulator with elastic suspension," *IEEE Trans. Robot.*, vol. 39, no. 6, pp. 4820–4836, Aug. 2023.

[17] M. A. Perozo, E. Niddam, S. Durand, L. Cuvillon, and J. Gangloff, "Teleoperation of a suspended aerial manipulator using a handheld camera with an IMU," *IEEE Robot. Autom. Lett.*, vol. 10, no. 1, pp. 700–707, Jan. 2025.

IEEE Transactions on Automation Science and Engineering (T-ASE) paper, presented at ICRA 2026, Vienna, Austria.

[18] Y. S. Sarkisov, M. Jun Kim, A. Coelho, D. Tsetserukou, C. Ott, and K. Kondak, "Optimal oscillation damping control of cable-suspended aerial manipulator with a single IMU sensor," in *Proc. IEEE Int. Conf. Robot. Autom. (ICRA)*, May 2020, pp. 5349–5355.

[19] H. M. Omar, R. Akram, S. M. S. Mukras, and A. A. Mahvouz, "Recent advances and challenges in controlling quadrotors with suspended loads," *Alexandria Eng. J.*, vol. 63, pp. 253–270, Jan. 2023.

[20] D. Hashemi and H. Heidari, "Trajectory planning of quadrotor UAV with maximum payload and minimum oscillation of suspended load using optimal control," *J. Intell. Robotic Syst.*, vol. 100, nos. 3–4, pp. 1369–1381, Dec. 2020.

[21] K. Klausen, T. I. Fossen, and T. A. Johansen, "Nonlinear control of a multirotor UAV with suspended load," in *Proc. Int. Conf. Unmanned Aircr. Syst. (ICUAS)*, Jun. 2015, pp. 176–184.

[22] K. Klausen, T. I. Fossen, and T. A. Johansen, "Nonlinear control with swing damping of a multirotor UAV with suspended load," *J. Intell. Robotic Syst.*, vol. 88, nos. 2–4, pp. 379–394, Dec. 2017.

[23] P. Chang, S. Yang, J. Tong, and F. Zhang, "A new adaptive control design for a quadrotor system with suspended load by an elastic rope," *Nonlinear Dyn.*, vol. 111, no. 20, pp. 19073–19092, Oct. 2023.

[24] S. Li, T. T. H. Duong, and D. Zanotto, "In-flight cable length control for improved quadrotor-based suspended load transportation," *IEEE Robot. Autom. Lett.*, vol. 9, no. 1, pp. 667–674, Jan. 2024.

[25] H. Das, "Dynamic inversion control of quadrotor with a suspended load," *IFAC-PapersOnLine*, vol. 51, no. 1, pp. 172–177, 2018.

[26] A. Chandra and P. P. S. Lal, "Higher order sliding mode controller for a quadrotor UAV with a suspended load," *IFAC-PapersOnLine*, vol. 55, no. 1, pp. 610–615, 2022.

[27] A. Dietrich and C. Ott, "Hierarchical impedance-based tracking control of kinematically redundant robots," *IEEE Trans. Robot.*, vol. 36, no. 1, pp. 204–221, Feb. 2020.

[28] C. D. Bellicoso, F. Jenelten, P. Fankhauser, C. Gehring, J. Hwangbo, and M. Hutter, "Dynamic locomotion and whole-body control for quadrupedal robots," in *Proc. IEEE/RSJ Int. Conf. Intell. Robots Syst. (IROS)*, Sep. 2017, pp. 3359–3365.

[29] M. A. Hopkins, D. W. Hong, and A. Leonessa, "Compliant locomotion using whole-body control and divergent component of motion tracking," in *Proc. IEEE Int. Conf. Robot. Autom. (ICRA)*, May 2015, pp. 5726–5733.

[30] P. M. Wensing and D. E. Orin, "Improved computation of the humanoid centroidal dynamics and application for whole-body control," *Int. J. Humanoid Robot.*, vol. 13, no. 1, Mar. 2016, Art. no. 1550039.

[31] A. Rocchi, E. M. Hoffman, D. G. Caldwell, and N. G. Tsagarakis, "OpenSoT: A whole-body control library for the compliant humanoid robot COMAN," in *Proc. IEEE Int. Conf. Robot. Autom. (ICRA)*, May 2015, pp. 6248–6253.

[32] S. Fahmi, C. Mastalli, M. Focchi, and C. Semini, "Passive whole-body control for quadruped robots: Experimental validation over challenging terrain," *IEEE Robot. Autom. Lett.*, vol. 4, no. 3, pp. 2553–2560, Jul. 2019.

[33] J. Englsberger, A. Dietrich, G. Mesesan, G. Garofalo, C. Ott, and A. Albu-Schaeffer, "MPTC—Modular passive tracking controller for stack of tasks based control frameworks," in *Proc. 16th Robot., Sci. Syst. (RSS)*, Jul. 2020.

[34] G. Zambella, D. Caporale, G. Grioli, L. Pallottino, and A. Bicchi, "Composite whole-body control of two-wheeled robots," *IEEE Trans. Robot.*, vol. 41, pp. 2301–2321, 2025.

[35] H. Das and C. Ott, "Partial feedback linearization control of a cable-suspended multirotor platform for stabilization of an attached load," in *Proc. IEEE/RSJ Int. Conf. Intell. Robots Syst. (IROS)*, 2025.

[36] H. Das, M. N. Vu, T. Egle, and C. Ott, "Observer-based controller design for oscillation damping of a novel suspended underactuated aerial platform," in *Proc. IEEE Int. Conf. Robot. Autom. (ICRA)*, May 2024, pp. 8415–8421.

[37] P. Kokotović, H. K. Khalil, and J. O'reilly, *Singular Perturbation Methods in Control: Analysis and Design*. Philadelphia, PA, USA: SIAM, 1999.

[38] A. D. Dragan and S. S. Srinivasa, "A policy-blending formalism for shared control," *Int. J. Robot. Res.*, vol. 32, no. 7, pp. 790–805, Jun. 2013.

[39] C. Masone, M. Mohammadi, P. Robuffo Giordano, and A. Franchi, "Shared planning and control for mobile robots with integral haptic feedback," *Int. J. Robot. Res.*, vol. 37, no. 11, pp. 1395–1420, Sep. 2018.

[40] J. Park, W. Chung, and Y. Youm, "On dynamical decoupling of kinematically redundant manipulators," in *Proc. IEEE/RSJ Int. Conf. Intell. Robots Syst. Hum. Environ. Friendly Robots With High Intell. Emotional Quotients*, vol. 3, Oct. 1999, pp. 1495–1500.

[41] H. Das, B. K. Sæbø, K. Y. Pettersen, and C. Ott, "Hardware-in-the-loop simulation of vehicle-manipulator systems for physical interaction tasks," in *Proc. IEEE/RSJ Int. Conf. Intell. Robots Syst. (IROS)*, Oct. 2023, pp. 4390–4396.

[42] A. Dietrich et al., "Practical consequences of inertia shaping for interaction and tracking in robot control," *Control Eng. Pract.*, vol. 114, Sep. 2021, Art. no. 104875.

[43] M. Tognon and A. Franchi, "Omnidirectional aerial vehicles with unidirectional thrusters: Theory, optimal design, and control," *IEEE Robot. Autom. Lett.*, vol. 3, no. 3, pp. 2277–2282, Jul. 2018.

[44] M. Hamandi, F. Usai, Q. Sablé, N. Staub, M. Tognon, and A. Franchi, "Design of multirotor aerial vehicles: A taxonomy based on input allocation," *Int. J. Robot. Res.*, vol. 40, nos. 8–9, pp. 1015–1044, Aug. 2021.

[45] M. Hamandi, K. Sawant, M. Tognon, and A. Franchi, "Omni-plus-seven (O7+): An omnidirectional aerial prototype with a minimal number of unidirectional thrusters," in *Proc. Int. Conf. Unmanned Aircr. Syst. (ICUAS)*, Sep. 2020, pp. 754–761.

[46] G. Garofalo, N. Mansfeld, J. Jankowski, and C. Ott, "Sliding mode momentum observers for estimation of external torques and joint acceleration," in *Proc. Int. Conf. Robot. Autom. (ICRA)*, May 2019, pp. 6117–6123.

Hemjyoti Das (Graduate Student Member, IEEE) received the B.Tech. degree in electrical engineering from the National Institute of Technology, Silchar, India, in 2016, and the M.Sc. degree in aerospace engineering from Delft University of Technology, The Netherlands, in 2020. He is currently pursuing the Ph.D. degree in aerial robotics with the Automation and Control Institute, Vienna University of Technology, Austria. He was a Research Engineer with the University of Twente, The Netherlands, from 2018 to 2020. His research interests include passivity and optimization-based whole-body control and reinforcement learning for aerial robotic manipulation.

Grazia Zambella (Member, IEEE) received the bachelor's degree in biomedical engineering, the master's degree in robotics and automation engineering, and the Ph.D. degree in robotics and automation engineering from the University of Pisa, in 2015, 2019, and 2023, respectively. Her Ph.D. thesis was on whole-body balancing control and recovery strategies for two-wheeled and biped humanoids. During the Ph.D. degree, she collaborated with Italian Institute of Technology, Genoa, Italy, and the Research Center "E. Piaggio," Pisa, Italy. She spent six months abroad with German Aerospace Center (DLR), Weßling, Germany. In 2022, she participated in the "ANA Avatar Xprize" Competition with the Team Alterego of Italian Institute of Technology and the University of Pisa. She is currently a University Assistant (Post-Doctoral) with Technische Universität Wien, Vienna, Austria.

Christian Ott (Fellow, IEEE) received the Dipl.-Ing. degree in mechatronics from the University of Linz, Austria, in 2001, and the Dr.-Ing. degree in control engineering from Saarland University, Saarbrücken, Germany, in 2005. From 2014 to 2022, he was the Head of the Department for "Analysis and Control of Advanced Robotic Systems," Institute of Robotics and Mechatronics, DLR. He is currently a Full Professor of robotics with Technische Universität Wien, Vienna, Austria. His current research interests include nonlinear robot control, elastic robots, whole-body control, impedance control, and control of humanoid robots.